

A swallowable X-ray dosimeter for the real-time monitoring of radiotherapy

Received: 9 February 2022

Accepted: 15 March 2023

Published online: 13 April 2023

 Check for updates

Bo Hou^{1,10}, Luying Yi^{1,10}, Dehong Hu², Zichao Luo¹, Duyang Gao², Chao Li³, Bowen Xing⁴, Jiong-Wei Wang^{5,6,7}, Chuen Neng Lee^{5,6}, Rong Zhang⁴, Zonghai Sheng²✉, Bin Zhou⁴✉ & Xiaogang Liu^{1,6,8,9}✉

Monitoring X-ray radiation in the gastrointestinal tract can enhance the precision of radiotherapy in patients with gastrointestinal cancer. Here we report the design and performance, in the gastrointestinal tract of rabbits, of a swallowable X-ray dosimeter for the simultaneous real-time monitoring of absolute absorbed radiation dose and of changes in pH and temperature. The dosimeter consists of a biocompatible optoelectronic capsule containing an optical fibre, lanthanide-doped persistent nanoscintillators, a pH-sensitive polyaniline film and a miniaturized system for the wireless readout of luminescence. The persistent luminescence of the nanoscintillators after irradiation can be used to continuously monitor pH without the need for external excitation. By using a neural-network-based regression model, we estimated the radiation dose from radioluminescence and afterglow intensity and temperature, and show that the dosimeter was approximately five times more accurate than standard methods for dose determination. Swallowable dosimeters may help to improve radiotherapy and to understand how radiotherapy affects tumour pH and temperature.

Despite important progress in our understanding of the molecular pathogenesis of cancer, gastrointestinal malignancies remain among the leading causes of death worldwide^{1–3}. Radiotherapy alone or in combination with surgery, chemotherapy or immunotherapy can be beneficial in treating gastrointestinal cancers^{4–6}. Modern radiotherapy enables the efficient irradiation of tumour tissue while minimizing damage to healthy surrounding tissue. However, the risk of low efficacy remains a major challenge for radiotherapists, owing to patient heterogeneity, treatment uncertainty and variations in delivery modalities^{6–8}. In particular, it is extremely difficult to determine, in real time, the dose delivered and absorbed in the location of gastrointestinal

tumours. Moreover, the methods currently used for the monitoring of biochemical indicators, such as pH and temperature, are insufficient for the comprehensive evaluation of radiotherapy^{9–11}.

Although there are a few *in vivo* clinical dosimeters, including metal-oxide-semiconductor field-effect transistors, thermoluminescence sensors and optically excited films^{5,12–16}, most of them are placed directly on (or nearby) the patient's skin to estimate the dose absorbed in the target area. *In vivo* dosimetry with electronic portal imaging devices has been explored for treatment verification in two and three dimensions. There are high costs associated with this type of system, and photon attenuation can alter the dose to the patient,

¹Department of Chemistry, National University of Singapore, Singapore, Singapore. ²Institute of Biomedical and Health Engineering, Shenzhen Institute of Advanced Technology, Chinese Academy of Sciences, Shenzhen, China. ³Department of Spaceborne Microwave Remote Sensing System, Aerospace Information Research Institute, Chinese Academy of Sciences, Beijing, China. ⁴Department of Precision Instruments, Tsinghua University, Beijing, China. ⁵Department of Surgery, Yong Loo Lin School of Medicine, National University of Singapore, Singapore, Singapore. ⁶Nanomedicine Translational Research Programme, Centre for NanoMedicine, Yong Loo Lin School of Medicine, National University of Singapore, Singapore, Singapore. ⁷Cardiovascular Research Institute, Yong Loo Lin School of Medicine, National University of Singapore, Singapore, Singapore. ⁸Institute of Materials Research and Engineering, Agency for Science, Technology and Research, Singapore, Singapore. ⁹Center for Functional Materials, National University of Singapore Suzhou Research Institute, Suzhou, China. ¹⁰These authors contributed equally: Bo Hou, Luying Yi. ✉e-mail: zh.sheng@siat.ac.cn; zhoub@mail.tsinghua.edu.cn; chmlx@nus.edu.sg

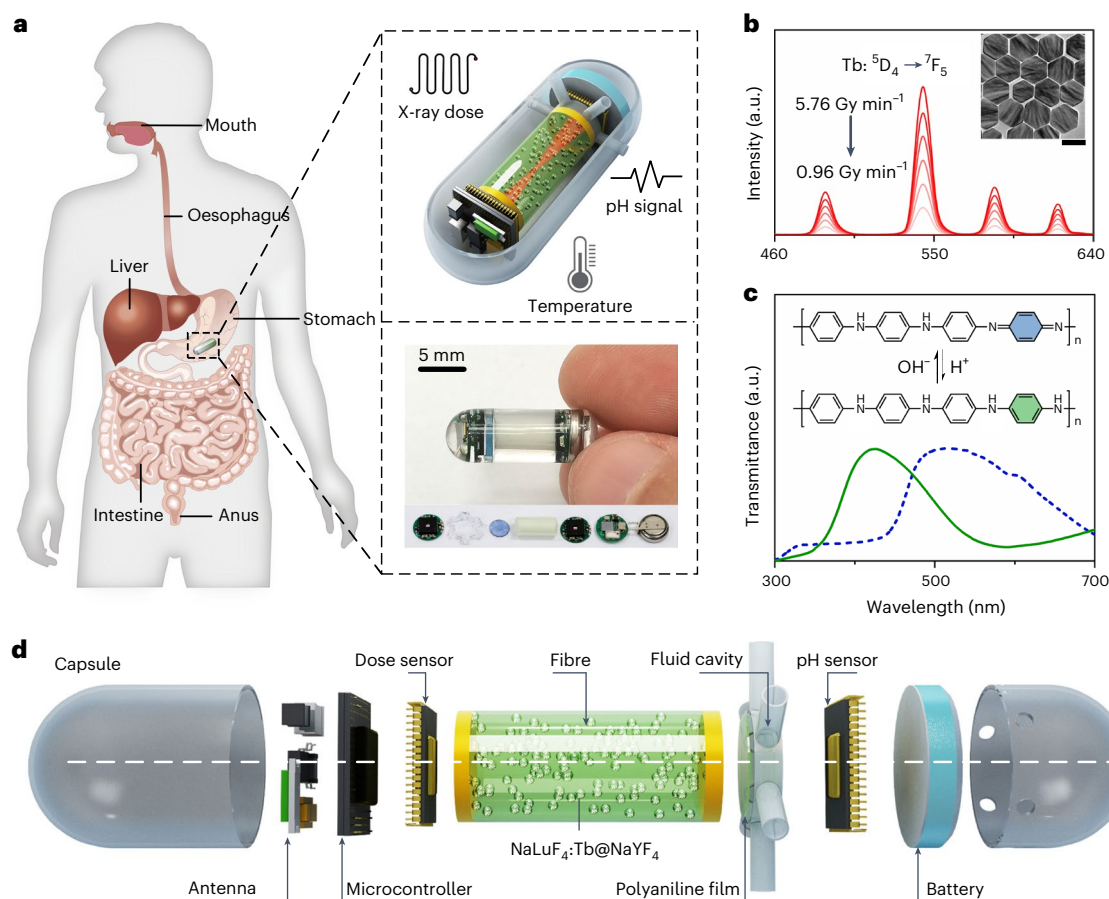


Fig. 1 | Design of a swallowable multimodal X-ray dosimeter. **a**, The dosimeter in schematic and real view, with the capacity for simultaneous in situ detection of absorbed radiation dose, pH and temperature in the gastrointestinal tract. **b**, Radioluminescence spectra of $\text{NaLuF}_4:\text{Tb}@NaYF_4$ nanoscintillators irradiated with different dose rates (0.96 to 5.76 Gy min^{-1}) at room temperature (inset: TEM image of as-synthesized nanoscintillators). Scale bar, 100 nm . **c**, Transmission spectra of the polyaniline film recorded in acidic and basic solutions. **d**, The all-in-one capsule dosimeter in exploded three-dimensional view. From left to right, the capsule consists of an antenna, an onboard microcontroller, a colour contrast sensor for dose detection, an optical fibre embedding persistent

$\text{NaLuF}_4:\text{Tb}@NaYF_4$ nanoscintillators, a pH-responsive polyaniline film, a multichannel fluid cavity, a colour contrast sensor for pH detection and a silver oxide battery. The radioluminescence propagates to both ends of the fibre in the form of total internal reflection. The dose is determined by the total intensity of the dose sensor, which measures light directly from the optical fibre, and the pH is measured by the colour contrast ratio of the pH sensor, which measures light after it passes through the polyaniline film. Photoelectric signals are processed by an integrated detection circuit and transmitted wirelessly to a mobile device for convenient reading.

either in the tumour or in normal tissue^{17,18}. Ingestible sensors offer notable opportunities for in situ monitoring of biochemical indicators^{19–21}. However, commercial ingestible sensors are mainly limited to pH and pressure sensors as well as to tethered capsules for imaging the oesophagus^{22–28}. Technological advancements in optics, electronics and especially materials science have provided new opportunities for developing an inexpensive, swallowable sensor that can simultaneously track biological indicators and X-ray dose absorption during gastrointestinal radiotherapy^{29–36}.

Design of swallowable X-ray dosimeters

Here we report the design and fabrication of a swallowable X-ray dosimeter capsule capable of measuring in situ physiological changes during gastrointestinal radiotherapy. The capsule comprises a flexible optical fibre encapsulated with $\text{NaLuF}_4:\text{Tb}@NaYF_4$ persistent nanoscintillators, a polyaniline film and a wireless miniaturized luminescence readout system. Capsule dimensions are $18 \text{ mm} \times 7 \text{ mm}$, approximately equivalent to a standard size 2 capsule commonly used for supplements and medicines (Fig. 1a). This capsule can respond linearly to irradiation of 50 kV ($0.04 \text{ mGy min}^{-1}$ to $16.68 \text{ mGy min}^{-1}$) or 6 MV (0.58 Gy min^{-1} to 5.76 Gy min^{-1}). The capsule also contains a built-in temperature sensor,

which provides correction factors to compensate for the effect of body temperature on the dosimeter, as well as an ambulatory pH sensor for the digestive system.

As a proof of concept, we first synthesized $\text{NaLuF}_4:\text{Tb}@NaYF_4$ core-shell nanoparticles according to a method described in the literature (Extended Data Fig. 1)³⁷. Upon X-ray irradiation, $\text{NaLuF}_4:\text{Tb}@NaYF_4$ nanoscintillators exhibited emission peaks at 489 , 546 and 584 nm (Fig. 1b). The intensity of the radioluminescence varied linearly with the X-ray dose. The afterglow of $\text{NaLuF}_4:\text{Tb}@NaYF_4$ nanoscintillators persisted for more than 30 d after the X-rays were turned off (Supplementary Table 1 and Video 1). Notably, the afterglow can be used as a self-sustaining light source to monitor dynamic pH changes within a few hours after irradiation, a capability not yet available with existing pH capsules. A transparent polydimethylsiloxane (PDMS) membrane was coated with pH-sensitive polyaniline to create the pH sensor. The absorption spectra of the polyaniline-coated film showed a high sensitivity to pH changes in the range 1 – 7 , which alters the transmission spectrum of radioluminescence after it passes through the coated film covering the capsule (Fig. 1c).

Apart from the $\text{NaLuF}_4:\text{Tb}@NaYF_4$ -encapsulated optical fibre and pH-sensitive polyaniline coating, the capsule also includes a custom

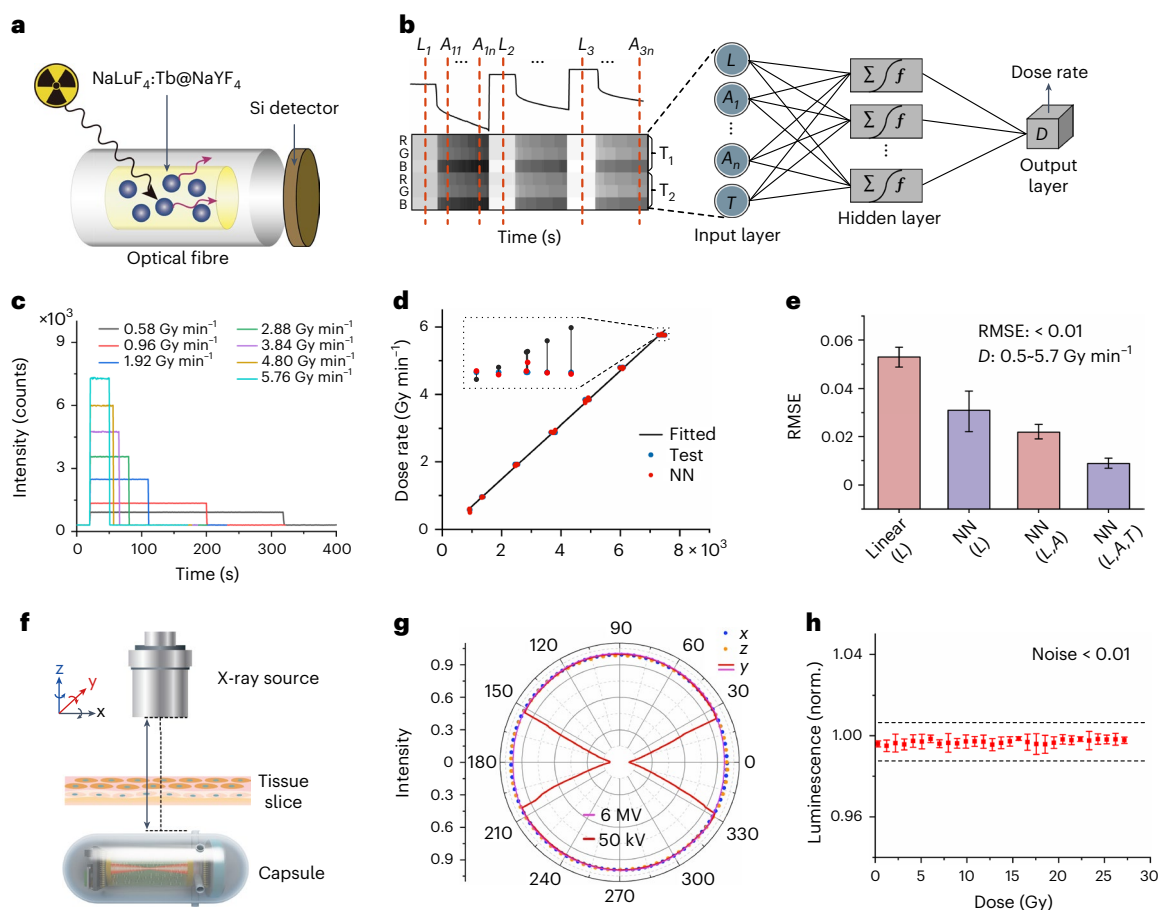


Fig. 2 | Operating principle and characterization of the capsule dosimeter.

a, Dosimetry monitoring diagram. Radiation dose is determined by measuring radioluminescence at the optical fibre's end, which contains radiation-sensitive materials (NaLuF₄:Tb@NaYF₄ nanoscintillators). **b**, Flowchart of the NN regression algorithm for dose determination. The trained NN model is fed with the feature parameters required for NN regression retrieved from the raw data, and the network then outputs the dose rate value. Feature parameters include radioluminescence (L), time-dependent afterglow (A_i , i represents time) and temperature (T). T_1 and T_2 represent different temperatures. **c**, Measured radioluminescence intensity over time at a dose of 2.88 Gy and dose rates from 0.58 to 5.76 Gy min⁻¹. **d**, **e**, Comparison of the accuracy of dose estimation using different algorithms (**d**) and feature parameter selection approaches (**e**). The inset in **d** shows a magnified view of the data at a dose rate of 5.76 Gy min⁻¹; the blue dots depict the actual dose rate versus radioluminescence in the test, the

black line or dots depict the dose assessment value obtained by linear fitting only from the parameter L , and the red dots depict the dose assessment value produced by the linear fitting algorithm fed with L and the NN algorithm fed with three parameter selection schemes as summarized in **e**. Each algorithm is cyclically executed 200 times to count accuracy. L represents the average intensity during irradiation. **f**, Schematic of the calibration test for determining dosage in various irradiation orientations. **g**, Light intensity normalized in different directions at the same dose rate. Under 50 kV and 6 MV irradiation, the anisotropy of angular response of the capsule is less than 80% and 3.2%, respectively. **h**, Normalized radioluminescence intensity as a function of dose under 6 MV irradiation at a dose rate of 5.76 Gy min⁻¹. In **e** and **h**, bar plots and error bars show the mean \pm s.d. The data in **e**, **g** and **h** were obtained from one capsule.

fluidic module with multiple inlets for dynamic gastric fluid sampling, two colour sensors for light and temperature measurements, a printed circuit board with a microcontroller and a button-sized silver oxide battery (Fig. 1d). At both ends of the optical fibre, two high-sensitivity colour sensors are installed. In the fibre, the radioluminescence propagates to both ends as total internal reflection. Changes in the intensity of the dosage sensor, which monitors light directly from the optical fibre, determine the dose. The pH, on the other hand, is determined by the colour contrast ratio of the pH sensor, which analyses light after it has passed through the pH-responsive film coating the capsule. An integrated detection circuit processes photoelectric signals, which are then wirelessly transmitted to a mobile phone for easy viewing.

Dose response of NaLuF₄:Tb@NaYF₄ nanoscintillators

We next evaluated the dose response of the optical fibre with embedded NaLuF₄:Tb@NaYF₄ nanoscintillators (Fig. 2a and Extended Data Figs. 2–4).

The radioluminescence intensity of NaLuF₄:Tb@NaYF₄ nanoscintillators varies linearly with the dose rate of low-energy X-rays (<50 kV) or high-energy irradiation (6 MV and 10 MV) and exhibits strong persistent luminescence. Both radioluminescence and afterglow intensities of NaLuF₄:Tb@NaYF₄ nanoscintillators are directly proportional to dose variations, implying that combining the two data types will lead to a more precise estimate of the absorbed dose. This X-ray dosimetry method also takes into account the effects of temperature on the nanoscintillators' radioluminescence and afterglow. To capture the complex relationship between the absorbed dose rate (D) and radioluminescence (L), afterglow with time (A_i , i represents time) and temperature (T), we used a machine learning technique based on a neural network (NN) regression for high-precision evaluation (Fig. 2b and Extended Data Fig. 5). For training data collection, the scintillators were irradiated with the same X-ray dose, but different dose rates (Fig. 2c). We tested two different algorithms: one based on a simple linear regression with only L as input and the other on an NN with L , A_i

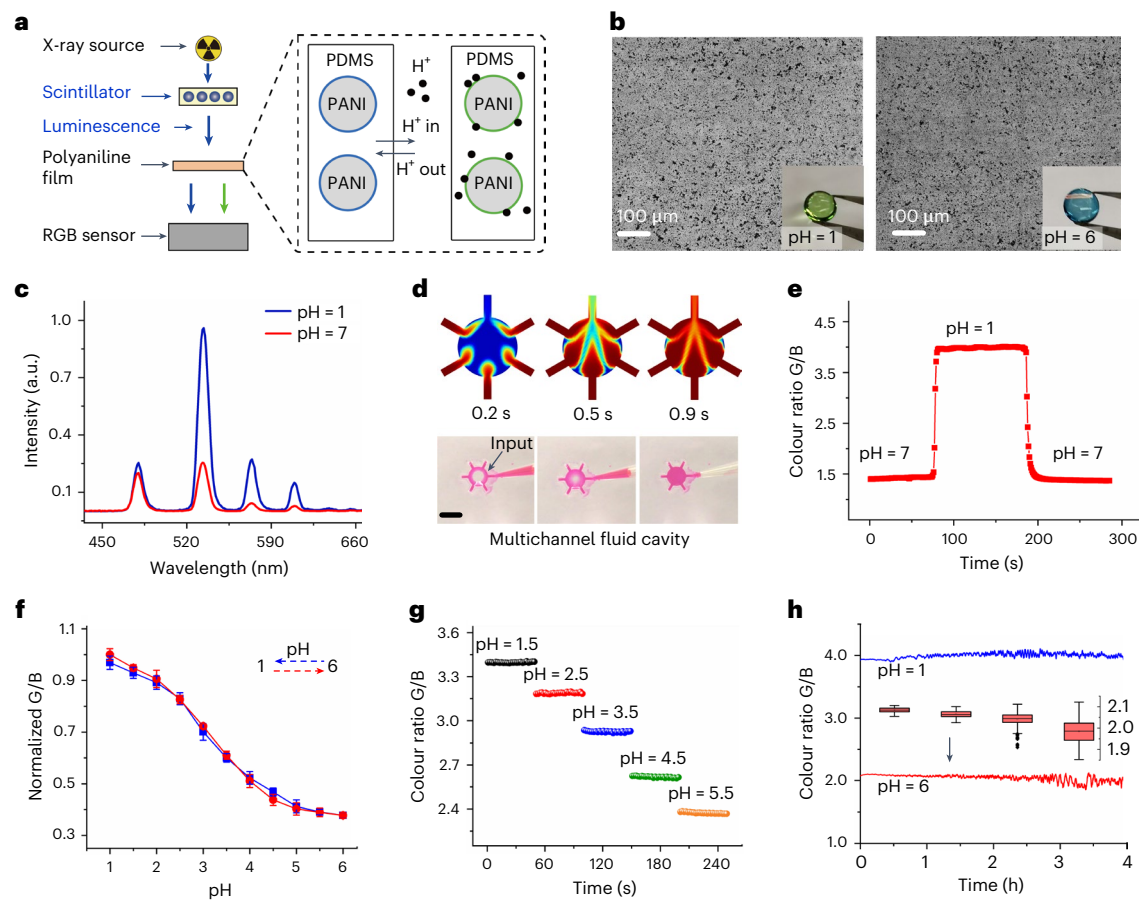


Fig. 3 | Characterization of pH sensing with a multichannel fluid cavity.

a, Principal working diagram of the optical pH sensor. The inset shows a model of the polyaniline (PANI) and H^+ locus on the PDMS film. **b**, Micrographs and photographs of a polyaniline film immersed in pH 1 and pH 6 solutions. **c**, Radioluminescence transmission spectrum after passing through the pH-sensitive film immersed in solutions of various pH values. **d**, Simulations and photographs of solution dispersion in a multichannel fluid cavity at different times (inlet flow rate, 1 ml min^{-1}). The time it takes for the fluid inside the cavity to exchange with the external fluid is less than 1 s. Scale bar, 4 mm. **e**, Dynamic evaluation of pH sensing. The sensor's response time can be as fast as 5 s when the pH of the solution changes suddenly. **f**, Normalized colour ratio G/B versus pH. The red line depicts the change in colour ratio G/B as pH is increased from

1 to 6, while the blue line depicts the opposite test result. Error bars represent the standard deviation of colour ratios. **g**, Variation in colour ratio G/B versus time as pH is altered from 1.5 to 5.5 in 0.5 steps. **h**, Persistent luminescence for pH sensing demonstration. The colour ratio G/B was plotted versus time after the radiation source was turned off at pH 1 (blue line) and pH 6 (red line). At the first, second, third and fourth hours after irradiation ceased, the interquartile range of the colour ratio was 2.6%, 3.8%, 7.1% and 12%, respectively. The minima, maxima, centre, bounds of the box and whiskers, and percentiles are marked in boxplots. The box range represents the interquartile range (IQR) of the data. The range between the upper and lower error bars represents 1.5IQR, and the line in the middle of the box is the median line. Whiskers represent outliers in the data. The data in **c–h** were obtained from one capsule.

and T as input (Fig. 2d,e). For dose rates up to 5.76 Gy min^{-1} , the root mean square error of the NN is less than 0.01 Gy min^{-1} (approximately 0.2%), which is approximately five times lower than the linear regression. It is worth noting that alternative input settings might be chosen depending on the application's needs. The real-time data L and T , for example, can be fed into the NN algorithm to calculate the real-time dose rate D without taking into account the afterglow A_i . The angular dependence of the capsule as a dosimeter was also evaluated, and the maximum difference in angular response for the 6 MV irradiation was 3.2% (Fig. 2f,g and Extended Data Fig. 6). Furthermore, the stability of the dosimeter was investigated by irradiating scintillators continuously for 5 min at a dose rate of 5.76 Gy min^{-1} . The results showed that the amplitude fluctuations of radioluminescence are less than 1% (Fig. 2h), indicating that the dosimeter is operationally stable. Although the NN algorithm calibrates the effect of temperature on luminescence and the contribution of afterglow to dose assessment, capsule dosimeters will require a detailed calibration that explicitly takes into account all parameters needed to convert the optical signal into an absorbed dose before they can be used clinically.

pH sensitivity of the polyaniline film

We next examined the pH sensitivity of the polyaniline-modified film (Fig. 3a,b and Extended Data Fig. 7). The capacity to estimate the pH profile in situ with accuracy and reliability is critical for early tumour diagnosis and monitoring the efficacy of cancer therapy^{38–40}. The transmitted light has a different G/B colour ratio than the radioluminescence that goes through the pH-sensing film immersed in different pH solutions (Fig. 3c). To improve temporal resolution for pH measurements, we designed a fluidic module with multiple inlets that can constantly provide fluid. The time it takes for the solute concentration in the reservoir to adjust to the new concentration (the refresh time) is a key performance indicator of the fluidics module in reaction to the inflow of solutions with a new solute concentration. The refresh time of the module was determined via numerical simulations (Fig. 3d). For six inlets with an inlet flow rate of 1 ml min^{-1} , the density and viscosity coefficient of gastric fluid were set to $1,000 \text{ kg m}^{-3}$ and $60 \text{ Mpa}\cdot\text{s}$, respectively, and the refresh time of the new solution concentration at 95% was less than 1 s. The pH-sensitive film was exposed to the solution and the colour ratio changed within 5 s of the solution pH change

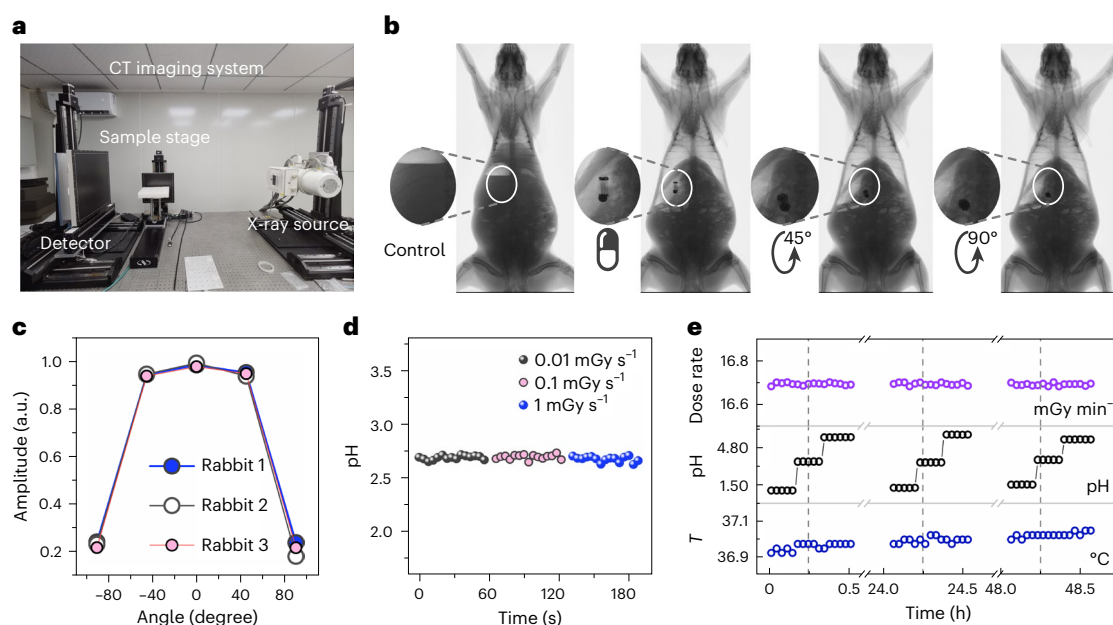


Fig. 4 | In vivo validation of dose assessment, pH sensing and stability. **a**, Photographs of the computed tomography imaging setup. **b**, After meticulous surgical dissection, the wireless capsule was placed at various angles in the stomach of the sedated rabbit. **c**, Capsule intensity versus angle in three separate

rabbits. **d**, Measured pH value versus time at various dose rates. **e**, Real-time, continuous in vitro measurement of radiotherapy dose, solution pH and temperature during a radiotherapy cycle to ensure stability.

(Fig. 3e). The response curve of the pH-sensitive film was obtained by plotting the colour ratio G/B of the transmitted light versus the pH of the prepared standard solution. The average responsivity was 20% for pH variations of 1 (measured by the average value of the slope divided by the range of the colour ratio G/B ; Fig. 3f). It is noteworthy that the response of the pH-sensitive film is reversible. We also tested the stability of the pH sensor in a variety of pH solutions (Fig. 3g). Furthermore, we demonstrated that the afterglow may be used to track pH changes after irradiation. The pH sensor responds quickly, accurately and consistently, with a sensitivity of 18.3% for pH variations of 1. The interquartile range of the colour ratio was 2.6%, 3.8%, 7.1% and 12%, respectively, at the first, second, third and fourth hours after irradiation ceased, demonstrating that the capsule may detect pH changes of 0.5 by afterglow even 4 h after radiotherapy (Fig. 3h).

Integration and demonstration of wireless capsules

We next integrated our X-ray dose and pH sensors with a wireless transmission platform. Most in vivo luminescence detection devices require external wiring and are limited to laboratory use, while a low-power wireless alternative could make in vivo detection more convenient. We created a wireless readout capsule that is fully integrated, miniaturized, and capable of monitoring the absorbed dose and detecting changes in biochemical indicators in the gastrointestinal tract in real time (Extended Data Fig. 8 and Supplementary Video 2). This system consists of a 1.6 g biocompatible plastic capsule with a diameter of 7 mm and a length of 18 mm. To extend the lifetime of the capsules for measuring absorbed dose and pH to more than 3 d, the system was designed to include a sleep state, a Bluetooth state and a work state, with the circuits in the sleep state most of the time. In each of the three states, power consumption is 6.3 μW (1.9 μA , 3.3 V), 660 μW (200 μA , 3.3 V) and 9.57 mW (2.9 mA, 3.3 V). We designed the temperature field distribution of the circuit to minimize the temperature rise to less than 0.03 $^{\circ}\text{C}$ to reduce the impact of heat generated by the circuit on biological tissue. We also developed a mobile phone application (App) to keep track of the capsule's status.

The capsule was characterized in a chamber with artificial gastric fluid initially (Extended Data Fig. 9 and Supplementary Video 3). We first determined the accuracy of the calibration curve that converts system performance to total dose absorbed by the capsule and gastric fluid pH. For the pH and dose measurements, we obtained average prediction errors of 0.13% and 0.3%, respectively. The smallest dosage prediction difference that could be detected was 1.8 $\mu\text{Gy min}^{-1}$. The smallest pH change that could be detected was 0.02, which corresponded to a colour ratio difference of 0.009 in the sensor output. This points to the capsule's great reliability in terms of dose and pH analysis in the digestive system. Additionally, an external X-ray source that could penetrate porcine tissue slices of varying thickness in 2 mm increments was used to provide X-ray doses of 24, 28 and 32 $\mu\text{Gy s}^{-1}$, with the capsule positioned beneath the tissue. An exponential function with depth can be effectively matched to the absorbed dose measured by the capsule.

Radiation monitoring in rabbit models

The dose assessment, pH sensing and operational stability were all validated in vivo. Adult rabbits ($n = 3$) were intubated and ventilated after being anaesthetized. The stomach was dissected meticulously, and wireless electronic capsules were inserted at various angles into the stomach. The stomach, as well as the overlying muscles and skin, were adjusted and sutured with care. The position and angle of the capsule were imaged using a computed tomography scanner (Fig. 4a,b). For fine alignment, the X-ray source was attached to a micromanipulator. We first tested angular dependence (Fig. 4c) and then demonstrated that pH values were unaffected by changes in absorbed dose rate or X-ray irradiation angle (Fig. 4d). The irradiation source voltage was less than 200 kV, which explains the huge disparity in angular response. Importantly, the capsule can operate in vitro for more than 72 h without large dosage or pH sensitivity loss, enabling sufficient time for measurements during clinical gastrointestinal passage (Fig. 4e).

We next tested the clinical feasibility of the wireless optoelectronic system for monitoring absorbed dose and pH in a physiologically relevant big animal model. The data were transmitted to a mobile phone and uploaded to cloud servers (Fig. 5a). Endoscopic and radiographic

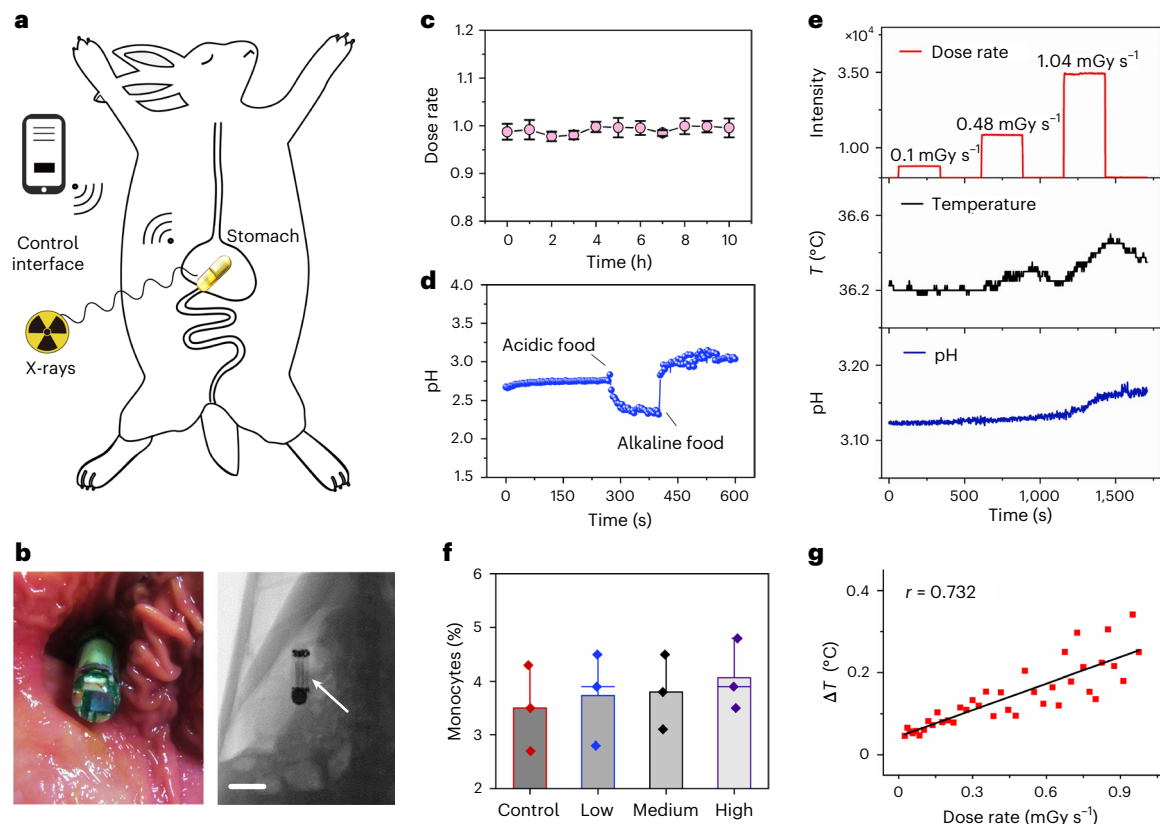


Fig. 5 | Characterization of absolute radiation dose, pH and temperature in the stomach of rabbits using the capsule dosimeter. a, Experimental setup consisting of an X-ray source and an inserted capsule dosimeter connected to a mobile phone through wireless transmission. **b,** Endoscopic (left) and radiographic (right) images showing the capsule's position in the stomach (scale bar, 1.2 cm). **c,** In situ monitoring of dose rate versus time; error bars represent the standard deviation of dose rate. $n = 3$ animals. **d,** In situ monitoring of pH versus time when the rabbit was fed acidic and then alkaline diets. **e,** Compilation

of data on radioluminescence intensity, pH and temperature alterations in response to irradiation. **f,** Monocyte percentage in experimental animals receiving different doses. Bar plots and error bars show the mean \pm s.d. Twelve male rabbits were randomly assigned into four groups (control, high dose, medium dose and low dose groups). **g,** Correlation between absorbed dose and temperature changes. Linear fitting was used to determine the correlation coefficient.

images revealed the precise position of the capsule in the stomach (Fig. 5b). Within 10 h post-insertion, the capsule was irradiated multiple times at a set dose rate. The determined dose rate varied by a maximum of 1.5%, which was due to capsule movement in the stomach or unstable irradiation (Fig. 5c). Similarly, the wireless electronic capsule was capable of detecting changes in the pH of the rabbit's gastric fluid following consumption of acidic and alkaline diets (Fig. 5d).

We delivered irradiation to the stomachs of the animals using a progressive X-ray dose rate. Our wireless dosimeter accurately determined the dose of radiation in the stomach, as well as minute changes in pH and temperature, in real time (Fig. 5e). The capsule inserted in the gastrointestinal cavity was capable of rapidly detecting changes in pH and temperature near irradiated organs. The difference in the percentage of monocytes found in animals receiving different doses further proved the difference in the stomach-specific X-ray dose administered (Fig. 5f). The receiving component (mobile phone App) can communicate with numerous electronic capsules simultaneously, allowing radiotherapists to manage data for multiple patients while also providing training data for the NN algorithm. The absorbed dose was correlated with variations in pH and temperature using data from multiple capsules (Fig. 5g and Extended Data Fig. 10). By linear fitting, we determined a correlation coefficient of 0.732 between the absorbed dose and the temperature change. At an absorbed dose of 1.037 mGy s^{-1} , the capsule detected an increase in temperature of nearly $0.3 \text{ }^{\circ}\text{C}$. It was verified that X-ray irradiation increased the pH of the stomach.

Discussion

The coupling of lanthanide-doped persistent nanoscintillators with an integrated temperature sensor and two independent colour sensors enables the construction of ingestible multimodal X-ray dosimeters that can simultaneously measure absorbed dose, pH and temperature in real time and in vivo. For practical applications, ultrasound or computed tomography scanning can be used to identify the position and posture of the capsule after it has been ingested. It is necessary to develop a positioning system to anchor and place the capsule at the target site. Moreover, swallowable dosimeters must be calibrated more accurately before clinical use. For instance, it is necessary to determine the dose-deposition conversion relationship between $\text{NaLuF}_4:\text{Tb}@\text{NaYF}_4$ nanoscintillators and tissues, as well as the calibration factor that accounts for Compton scattering and pair production.

The capsule dosimeter with pH and temperature measuring capabilities was developed primarily for gastrointestinal tumours. For example, it can be used to evaluate the in situ absorbed dose during radiotherapy for gastric cancer, which is important because the stomach and some surrounding organs (such as the liver, kidney and spinal cord) are dose-limiting. Along with assessing the absolute dose absorbed in the gastrointestinal tract, the capsule dosimeter is designed so that it can also be coupled to image-guided and intensity-modulated radiation to monitor treatment in different malignancies. For example, it can be easily put into the rectum to monitor

prostate cancer brachytherapy. Moreover, with further optimization of the capsule's size, it could be placed in the upper nasal cavity to enable accurate and real-time measurements of the absorbed dose in nasopharyngeal or brain tumours, thereby minimizing radiation damage and potential side-effects to surrounding structures. Furthermore, the technology may facilitate the development of highly sensitive in vivo sensors for gas molecules, reactive oxygen species and other physiological or biochemical indicators. The integration of persistent nanoscintillators with electronics raises the possibility of improving quality control and, ultimately, of enhancing the care provided to cancer patients undergoing radiotherapy.

Methods

Animal experiments were conducted in accordance with the protocol approved by the Animal Care and Use Committee of the Shenzhen Institute of Advanced Technology, Chinese Academy of Sciences.

Materials and reagents

Yttrium(III) acetate hydrate ($\text{Y}(\text{CH}_3\text{CO}_2)_3 \cdot x\text{H}_2\text{O}$, 99.9%), lutetium(III) acetate hydrate ($\text{Lu}(\text{CH}_3\text{CO}_2)_3 \cdot x\text{H}_2\text{O}$, 99.9%), terbium(III) acetate hydrate ($\text{Tb}(\text{CH}_3\text{CO}_2)_3 \cdot x\text{H}_2\text{O}$, 99.9%), sodium hydroxide (NaOH, >98%), ammonium fluoride (NH_4F , >98%), 1-octadecene (ODE, 90%), oleic acid (OA, 90%), aniline ($\text{C}_6\text{H}_5\text{NH}_2$, 99.5%), ammonium persulfate ($(\text{NH}_4)_2\text{S}_2\text{O}_8$, 99.5%), hydrochloric acid (HCl, 36%) and cyclohexane (chromatography grade, 99.7%) were purchased from Sigma-Aldrich. SYLGARD 184 silicone elastomer kit was purchased from Dow Corning. $\text{SrAl}_2\text{O}_4:\text{Eu}^{2+}/\text{Dy}^{3+}$ and $\text{ZnS}:\text{Cu}^{2+}$ phosphorus powders were purchased from Xiucui Chemical. UV-curable single-component liquid adhesive NOA81 was purchased from Norland Products. EA E-30CL epoxy was purchased from Loctite. The capsule cap was purchased from Huasheng Biopharmaceutical.

Synthesis and characterization of $\text{NaLuF}_4:\text{Tb}@ \text{NaYF}_4$ core-shell nanocrystals

$\text{NaLuF}_4:\text{Tb}$ nanocrystals were synthesized by co-precipitation. After bringing the reaction mixture to room temperature, nanocrystals were precipitated with ethanol, centrifuged, collected and stored at 4 °C in a refrigerator. $\beta\text{-NaLuF}_4:\text{Tb}@ \text{NaYF}_4$ core-shell nanocrystals were prepared by epitaxial growth of as-prepared core nanocrystals. Transmission electron microscopy (TEM) images were taken using a Tecnai G2 F20 S-TWIN microscope (FEI Nanoports). The sample composition was determined by energy dispersive X-ray spectroscopy operated with a Bruker model A300 spectrometer. X-ray powder diffraction was performed using an X-ray powder diffractometer (D/MAX-3C, Rigaku). Radioluminescence spectra and persistent luminescence decay curves were measured using an Edinburgh FS5 fluorescence spectrophotometer (Edinburgh Instruments) equipped with a miniature X-ray source (Amptek) (Extended Data Fig. 1)⁴¹.

Fabrication of the optical fibre embedded with $\text{NaLuF}_4:\text{Tb}@ \text{NaYF}_4$ nanocrystals

In a typical experiment, the SYLGARD 184 silicone elastomer base was premixed with the curing agent (10:1 by mass). A cyclohexane solution of $\text{NaLuF}_4:\text{Tb}$ (15 mol%)@ NaYF_4 nanocrystals was added to the solution and stirred vigorously. The resulting mixture was poured into a tube mold. The resulting composites were degassed in a vacuum container to remove air bubbles. The mixture was finally heated at 80 °C for 30 min. After bringing the core to room temperature, it was extracted using water pressure. Furthermore, the core was wrapped with a layer of silicone gel. Ray-optical simulations showed that the fibre's small fibre diameter leads to a large detectable power when the luminous core is located in the centre of the fibre and coaxial with the colour sensor. As a result, the optical fibre was optimized to have a diameter of 3 mm and was equipped with a radioluminescence core in the centre.

Characterization of the optical fibre-based dosimeter

The dosimeter's characterization and angular dependence were performed on a motorized rotating table (Daheng Optics, GCD-011060M). The sensor response was recorded using a fibre optic spectrometer (Ocean Optics QE Pro) or a colour sensor chip (AS73211). Thermally stimulated luminescence was measured on a ceramic hot plate (Thermo Fisher) and the temperature was also monitored with a temperature sensor integrated into the colour sensor chip. The dynamic characteristics of the fibre-based dosimeter were tested by placing an X-ray chopper behind the X-ray source. The luminescence properties of $\text{NaLuF}_4:\text{Tb}@ \text{NaYF}_4$ nanoscintillators under high-energy radiation (6 MV and 10 MV) were tested using a medical radiotherapy machine (TrueBeam, Varian) at the Singapore National Cancer Centre.

Dose estimation

Raw data include time series of CIE spectral tristimulus values (X , Y , Z) and temperature T . The sum of the X , Y and Z values was used to determine the radioluminescence intensity L and the afterglow intensity A_i (i represents time) at different time points. The capsule was exposed to X-rays at various dose rates from 1 mGy min^{-1} to 16.68 mGy min^{-1} (excitation voltage 50 kV, excitation current 5 μA –80 μA , interval 5 μA), and the temperature was increased from 32 °C to 46 °C in 2 °C increments. There were over 3,000 data points, with 75% of the data fed into each algorithm for training. The trained models were used to predict the remaining 25% of the data. We compared the prediction accuracy of the linear regression, linear support vector machine (SVM) algorithm and NN regression algorithms. We also compared the accuracy of prediction for four different parameter selection strategies: (1) L , (2) L and T , (3) L and A_i , and (4) L , A_i and T .

The linear regression, linear SVM and NN algorithms were included in the Regression Learner and Neural Network Fitting application toolboxes in MATLAB 2020. A two-layer feed-forward network with sigmoidal hidden neurons and linear output neurons was used for the NN. This NN has an input layer with 1–5 nodes (depending on the feature parameter strategy) and a hidden layer with 5 nodes. The network was trained using the Levenberg-Marquardt backpropagation algorithm, with the sigmoid function as the activation function. A linear SVM model with linear kernel function was used in the SVM algorithm. The linear SVM algorithm had a larger root mean square error (RMSE) than the others. When L , A_i and T were specified as feature parameters simultaneously, the results of the NN fitting algorithm had a reduced RMSE. Finally, data (L , A_i , T) were selected as feature parameters to be input into the NN fitting algorithm to predict the dose rate.

Fabrication of pH-sensitive polyaniline film

A circular PDMS film with a diameter of 5 mm, thickness of 0.2 mm and high optical transmittance was selected as the substrate. In a volume ratio of 1:11 (hydrochloric acid:deionized water), 37% concentrated hydrochloric acid (12 mol l^{-1}) was diluted to 1 mol l^{-1} with deionized water. To make 0.05 mol l^{-1} aniline solution, 210 mg of aniline solution and 1 mol l^{-1} hydrochloric acid solution were mixed. Solid ammonium persulfate was mixed with 1 mol l^{-1} hydrochloric acid solution and thoroughly agitated to obtain 0.05 mol l^{-1} ammonium persulfate solution. The film was cleaned before being immersed in aniline solution^{42,43}. Within 3 min, the same volume of ammonium persulfate solution was added and allowed to react for 20 min at 20 °C. The reaction vessel was gently shaken every 5 min throughout the reaction to ensure uniform deposition of reactants on the film surface. The film was rinsed with 1 mol l^{-1} hydrochloric acid after it was removed. After repeating the above steps for further polymerization, the film was thoroughly washed with water to eliminate any unbound polyaniline.

Characterization of photochemical pH sensor

Transmission spectra of the pH sensor film in solutions with different pH values were measured using a spectrophotometer (Cary Series

UV-Vis-NIR, Agilent)⁴⁴. A microsyringe pump (LSP02-1B, Longer Precision Pump) was used to change the pH by constantly pumping an equivalent volume of NaOH solution into the hydrochloric acid solution. All pH calibrations were performed using a digital pH-3c pH meter (INESA Scientific). The radioluminescence guided by the optical fibre containing NaLuF₄:Tb@NaYF₄ nanoscintillators was incident on the pH sensor film immersed in the solution, where the transmitted light was measured by the colour sensor chip. The sensor continued to operate after the X-ray source was turned off, recording the afterglow emission that passed through the pH film. The sensor's stability was evaluated by measuring the colour sensor's G/B response in a pH 3.5 solution at room temperature for 30 h. The kinetic assay indicates that the probe responds promptly to pH changes and is stable to dose rate changes.

Fabrication and characterization of the multichannel fluid cavity

The three-dimensional (3D)-printed fluid cavity has a reservoir and multiple inlets. The cylindrical reservoir is 2.3 mm in radius and 1.6 mm thick. The inlet channels are 1.2 mm long and 0.8 mm wide. The cylindrical container's two layers are coated with a thin layer (200 μm) of polyaniline. The fluid cavity refresh time was simulated, and the same device geometry was used to construct a 3D model. The Stokes equation for an incompressible flow was solved numerically using COMSOL Multiphysics 5.6 finite-element software. The solute concentration in the chamber was tracked by computing the average concentration over the bottom surface of the chamber. The channel was set to have six inlets, each with a flow rate of 0.2 ml min⁻¹ and no-slip boundary conditions on all channel walls. The simulated 95% refresh time is ~1 s.

Characterization of temperature

In addition to the dose and pH, the temperature was measured concurrently. The measurement was stored in the colour sensor chip's registers, which is defined as T_d . The temperature measurement had a resolution of 12 bits and a step size of 0.05 Kelvin per bit, that is, 20 counts per K. The chip temperature measured in °C is equal to:

$$T = T_d \times 0.05 + 66.9^\circ \quad (1)$$

The 12-bit analog-to-digital converter has a high sampling rate of 1,000 samples per second, allowing precise and time-accurate measurements by taking the averages.

The impact of circuit heating on measured tissue temperatures can be greatly reduced by using a sensing circuit with a properly designed temperature field distribution. Once the capsule system is in place, the device must be heated during operation to ensure accurate temperature measurement. The temperature changes as a function of time and the three spatial coordinates in heat conduction, and this is accompanied by heat generation or heat consumption (circuit heating). Time-dependent heat conduction is called three-dimensional unsteady heat conduction, which can be described by the heat equation:

$$\frac{\partial}{\partial x} \left(k \frac{\partial T}{\partial x} \right) + \frac{\partial}{\partial y} \left(k \frac{\partial T}{\partial y} \right) + \frac{\partial}{\partial z} \left(k \frac{\partial T}{\partial z} \right) + q = \rho c_p \frac{\partial T}{\partial t} \quad (2)$$

where t is the time; x , y and z are the spatial coordinates; ρ is the density; c_p is the specific heat capacity at constant pressure; and q represents the circuit's heat generation. The thermal diffusion equation states that the net rate of heat conduction into a unit volume plus the unit rate of heat generation of a volume must equal the rate of change of energy stored in a unit volume at any point in the medium. For the PCB material (RF-4, Jantao), thermal conductivity k equals 0.3 W m⁻¹ K and specific heat capacity c_p equals 650 J kg⁻¹ °C. Following calculation, the temperature rise caused by heat diffusion to the temperature sensor can be ignored, allowing the electronic capsule to accurately measure the environmental temperature.

Design and characteristics of the electric circuit

The system's main components include an ultra-low-power 5.0 Bluetooth chip DA14585, colour sensors AS73211 and a power supply chip TLV62569. For in vivo capsule applications, power consumption and volume are strictly limited. DA14585 is an ultra-low-power system on chip that includes a 2.4 GHz transceiver and an ARM Cortex-M0 microcontroller with 96 kb RAM and 64 kb one-time programmable memory. The optimized programme was downloaded to the one-time programmable memory for our application. As soon as the device is turned on, the programme begins to run. DA14585 has a transmit sensitivity of -20 dB and a receive sensitivity of -93 dB. AS73211 is a low-power, low-noise integrated colour sensor (4.5 mW, 3.0 V, 1.5 mA). It has a signal resolution accuracy of up to 24 bits and a radiation sensitivity of 0.5 pW cm⁻². I²C was used to connect the sensor to DA14585. To achieve high detection sensitivity, the circuit's digital and analogue grounds were separated to ensure that the noise of the root mean square voltage is less than 8 μV.

Power consumption calculation

The entire system runs on 3.3 V. A single TLV62569 regulator converts the lithium battery's 3.7–4.2 V range to a steady 3.3 V. After the programme starts, the capsule enters one of three states: sleep, pairing with Bluetooth and actively working. A 3.7 V lithium-ion battery (LIR0640, 10 mAh) powers the flexible printed circuit board (FPCB) during data acquisition and transmission. By sharing the I²C interface address, two AS73211 sensors are connected to a Bluetooth chip. The Bluetooth transceiver has a working current of 2.9 mA and a working time of 10 ms s⁻¹. The capsule's total power consumption in the working mode was calculated to be 9.57 mW on average. After the capsule has reached the working state, the user can return it to the Bluetooth state by pressing the 'STOP' button on the mobile phone App. Power consumption in the Bluetooth state was 0.2 mA, corresponding to a power consumption of 0.66 mW. Power consumption in the idle state was only 6.3 μW (1.9 μA, 3.3 V). Patients typically receive radiotherapy 5 times per week for 20–30 min per session (including radiation simulation and planning scans). As a result, the system can monitor the patient's radiation dose and physiological indicators for a week.

Design, fabrication and assembly of the electric capsule

The capsule's main components include a battery, an optical fibre, a pH detection cavity, a Bluetooth communication circuit, a dose detection circuit and a pH detection circuit. The three circuits were all built on a 200-μm-thick FPCB. For the Bluetooth communication circuit, the DA14585 Bluetooth chip (WLCSP 34 pins, 2.40 mm × 2.66 mm) and other chips were soldered to the FPCB. The FPCB was then placed in a reflow soldering machine (T-962A, Puhui) and cured for 5 min at 220 °C, which is lower than the melting point of the PCB material. Reflow soldering gave a good electrical connection to the circuit and was unaffected by solder bumps. Reflow soldering of the AS73211 RGB chip (QFN16, 4.0 mm × 4.0 mm) to the FPCB was also used to connect the pH detection and dosage detection circuits.

After the three PCBs were fabricated and soldered, they were put together. Before attaching the pH sensor to the RGB chip, we first used medical-grade UV-curable epoxy resin (NOA81, Norland) to attach the polyaniline-coated PDMS film to the 3D-printed multichannel fluid cavity. Assembly of other sensor components, such as X-ray sensitive optical fibres (3 mm × 8 mm), dose detection circuits and lithium button batteries (6 mm × 4 mm), was also performed using UV-curable epoxy resin.

Epoxy resin (EA E-30CL, Loctite) was applied to all connectors and module surfaces following assembly. Plasticine was used to seal the pH sensor's inlets, and all electrically connected parts were then placed inside the capsule cap. The final step was to place everything together in a standard size 2 capsule. For the final step, we used PDMS to fill the gap between the electronic components and the cap and cured it for 48 h at room temperature.

In vitro and ex vivo characterization

A miniature X-ray source with a maximum power of 4 W was used to undertake an in vitro evaluation of the capsule in a custom-built solution tank. The tank was placed on a stirring hot plate to maintain the solution temperature between 32 °C and 46 °C, and to mix the solution to speed up the rate of pH conversion. A microsyringe pump was used to add HCl to NaOH in the tank, and the pH was monitored using a commercial pH tester. Capsule efficacy was assessed in a pH-controlled fluid and in a fresh ex vivo porcine bone sample at 10 cm depth. A plastic holder was placed in the solution tank, and the wireless capsule was positioned between the porcine tissue sample and the plastic holder, fully immersed in the solution during the measurement. Because of the large divergence angle of the X-ray source and the absorption of porcine tissue, the dose delivered around the capsule was calibrated using a commercial dosimeter. The sensors in the capsule wirelessly send information about the dosage, pH and temperature to the host computer.

In vivo measurements

Male New Zealand white rabbits (90-day-old, 1.8–2.2 kg weight) were purchased from Qingdao Kangda Biotechnology. The rabbits were fasted the day before surgery. Sodium pentobarbital (4 ml kg⁻¹, 3%) was administered intraperitoneally to anaesthetize the rabbits after they were placed on their backs in a holding frame during surgery. After removing the rabbit's fur from the left side of its chest, we cleaned the region. After the stomach was cut open, six or eight stitches were used to suture the stomach wall and skin to form a circular area to prevent stomach contents from spilling into the abdominal cavity. Incisions were created in the stomach skin to aspirate a 5 cm section of stomach contents with a needleless syringe. Sterilized capsules were simply sutured into the stomach. The detector was removed after CT imaging and X-ray irradiation with various dosages, and a continuous full-layer suture was performed on the rabbit's stomach wall. The wound was sprinkled with sulfa crystal powder and slathered with fish gypsum ointment before being wrapped in bandage or gauze. Anti-inflammatory injections were given to the rabbits after surgery.

For routine blood testing, 12 male rabbits were randomly assigned into 4 groups (control, high dose, medium dose and low dose groups) and 5–10 ml of blood were collected from the hearts of anaesthetized rabbits 24 h after they were irradiated with varying dosages of X-rays to perform routine blood examinations. If blood could not be drawn, the position of the needle was adjusted back and forth, but the needle was not allowed to swing into the chest cavity to protect the heart and lungs.

Design of a customized mobile phone App

The capsule is controlled by a smartphone App, which provides a user-friendly interface for data display and collection. To use this App, the user must first turn on the capsule and then launch the App on the smartphone. Afterwards, the App and the capsule create a secure Bluetooth connection. As a result, the App can receive and display data stream from the capsule in real time. These data can be graphically displayed over time using the App. Data and graphs can be stored locally, uploaded to cloud servers and shared on social media. The current version was developed in the Android environment using Visual Studio 2015. Other popular operating systems, such as iOS, can readily support similar application interfaces.

Reporting summary

Further information on research design is available in the Nature Portfolio Reporting Summary linked to this article.

Data availability

The main data supporting the results in this study are available within the paper and its Supplementary Information. All data generated in this study, including source data and the data used to make the figures,

are available for research purposes from the corresponding author on reasonable request.

Code availability

The code is available from <https://github.com/yly1994/Swallowable-X-ray-Dosimeter-.git>.

References

- Steiger, C. et al. Ingestible electronics for diagnostics and therapy. *Nat. Rev. Mater.* **4**, 83–98 (2018).
- Huynh, E. et al. Artificial intelligence in radiation oncology. *Nat. Rev. Clin. Oncol.* **17**, 771–781 (2020).
- Mijnheer, B., Beddar, S., Izewska, J. & Reft, C. In vivo dosimetry in external beam radiotherapy. *Med. Phys.* **40**, 070903 (2013).
- Patel, R. B. et al. Low-dose targeted radionuclide therapy renders immunologically cold tumors responsive to immune checkpoint blockade. *Sci. Transl. Med.* **13**, eabb3631 (2021).
- Soliman, Y. S., El Gohary, M. I., Abdel Gawad, M. H., Amin, E. A. & Desouky, O. S. Fricke gel dosimeter as a tool in quality assurance of the radiotherapy treatment plans. *Appl. Radiat. Isot.* **120**, 126–132 (2017).
- Chaikh, A., Beuve, M. & Balosso, J. Nanotechnology in radiation oncology: the need for implantable nano dosimeters for in-vivo real time measurements. *Int. J. Cancer Ther. Oncol.* **3**, 3217 (2015).
- O'Keeffe, S. et al. A review of recent advances in optical fibre sensors for in vivo dosimetry during radiotherapy. *Br. J. Radiol.* **88**, 20140702 (2015).
- Dai, Y. H. et al. Radiosensitivity index emerges as a potential biomarker for combined radiotherapy and immunotherapy. *NPJ Genom. Med.* **6**, 40 (2021).
- Yang, Y. et al. A laser-engraved wearable sensor for sensitive detection of uric acid and tyrosine in sweat. *Nat. Biotechnol.* **38**, 217–224 (2020).
- Wang, C. et al. Monitoring of the central blood pressure waveform via a conformal ultrasonic device. *Nat. Biomed. Eng.* **2**, 687–695 (2018).
- Tang, B. et al. A near-infrared neutral pH fluorescent probe for monitoring minor pH changes: imaging in living HepG2 and HL-7702 cells. *J. Am. Chem. Soc.* **131**, 3016–3023 (2009).
- Zhuang, Q. et al. Embedded structure fiber-optic radiation dosimeter for radiotherapy applications. *Opt. Express* **24**, 5172–5185 (2016).
- Piermattei, A. et al. A National project for in vivo dosimetry procedures in radiotherapy: first results. *Nucl. Instrum. Methods Phys. Res. B* **274**, 42–50 (2012).
- Yu, G. et al. A discrete organoplatinum(II) metallacage as a multimodality theranostic platform for cancer photochemotherapy. *Nat. Commun.* **9**, 4335 (2018).
- Klein, D. et al. In-phantom dose verification of prostate IMRT and VMAT deliveries using plastic scintillation detectors. *Radiat. Meas.* **47**, 921–929 (2012).
- Tanderup, K., Beddar, S., Andersen, C. E., Kertzsch, G. & Cygler, J. E. In vivo dosimetry in brachytherapy. *Med. Phys.* **40**, 070902 (2013).
- Scarantino, C. W. et al. An implantable radiation dosimeter for use in external beam radiation therapy. *Med. Phys.* **31**, 2658–2671 (2004).
- Beyer, G. P. et al. An implantable MOSFET dosimeter for the measurement of radiation dose in tissue during cancer therapy. *IEEE Sens. J.* **8**, 38–51 (2008).
- Abramson, A. et al. Oral delivery of systemic monoclonal antibodies, peptides and small molecules using gastric auto-injectors. *Nat. Biotechnol.* **40**, 103–109 (2022).

20. Canales, A. et al. Multifunctional fibers for simultaneous optical, electrical and chemical interrogation of neural circuits in vivo. *Nat. Biotechnol.* **33**, 277–284 (2015).
21. Al-Rawhani, M. A., Beeley, J. & Cumming, D. R. Wireless fluorescence capsule for endoscopy using single photon-based detection. *Sci. Rep.* **5**, 18591 (2015).
22. Nadeau, P. et al. Prolonged energy harvesting for ingestible devices. *Nat. Biomed. Eng.* **1**, 0022 (2017).
23. Kalantar-Zadeh, K. et al. A human pilot trial of ingestible electronic capsules capable of sensing different gases in the gut. *Nat. Electron.* **1**, 79–87 (2018).
24. Ou, J. Z. et al. Potential of in vivo real-time gastric gas profiling: a pilot evaluation of heat-stress and modulating dietary cinnamon effect in an animal model. *Sci. Rep.* **6**, 33387 (2016).
25. Iacovacci, V. et al. A fully implantable device for intraperitoneal drug delivery refilled by ingestible capsules. *Sci. Robot.* **6**, eabh3328 (2021).
26. Abramson, A. et al. An ingestible self-orienting system for oral delivery of macromolecules. *Science* **363**, 611–615 (2019).
27. Mimee, M. et al. An ingestible bacterial-electronic system to monitor gastrointestinal health. *Science* **360**, 915–918 (2018).
28. Kimchy, Y. et al. Radiographic capsule-based system for non-cathartic colorectal cancer screening. *Abdom. Radiol.* **42**, 1291–1297 (2017).
29. Khutoryanskiy, V. V. Supramolecular materials: longer and safer gastric residence. *Nat. Mater.* **14**, 963–964 (2015).
30. Gora, M. J. et al. Tethered capsule endomicroscopy enables less invasive imaging of gastrointestinal tract microstructure. *Nat. Med.* **19**, 238–240 (2013).
31. Lee, H. et al. A graphene-based electrochemical device with thermoresponsive microneedles for diabetes monitoring and therapy. *Nat. Nanotechnol.* **11**, 566–572 (2016).
32. Sonmezoglu, S., Fineman, J. R., Maltepe, E. & Maharbiz, M. M. Monitoring deep-tissue oxygenation with a millimeter-scale ultrasonic implant. *Nat. Biotechnol.* **39**, 855–864 (2021).
33. Waltz, E. Drugs go wireless. *Nat. Biotechnol.* **34**, 15–18 (2016).
34. Qureshi, W. A. Current and future applications of the capsule camera. *Nat. Rev. Drug. Discov.* **4**, 447–450 (2004).
35. Smith, S., Oberholzer, A., Korvink, J. G., Mager, D. & Land, K. Wireless colorimetric readout to enable resource-limited point-of-care. *Lab Chip* **19**, 3344–3353 (2019).
36. Kim, T., McCall, J. G. & Jung, Y. H. Injectable, cellular-scale optoelectronics with applications for wireless optogenetics. *Science* **340**, 211–216 (2013).
37. Ou, X. et al. High-resolution X-ray luminescence extension imaging. *Nature* **590**, 410–415 (2021).
38. Ma, G. et al. pH-responsive nanoprobe for in vivo photoacoustic imaging of gastric acid. *Anal. Chem.* **91**, 13570–13575 (2019).
39. Nakata, S. et al. A wearable pH sensor with high sensitivity based on a flexible charge-coupled device. *Nat. Electron.* **1**, 596–603 (2018).
40. Anemone, A., Consolino, L., Arena, F., Capozza, M. & Longo, D. L. Imaging tumor acidosis: a survey of the available techniques for mapping in vivo tumor pH. *Cancer Metastasis Rev.* **38**, 25–49 (2019).
41. Berger, M. J. *Xcom: Photon Cross Sections Database* (NIST, 2013); <https://www.nist.gov/pml/xcom-photon-cross-sections-database>
42. Abu-Thabit, N., Umar, Y., Ratemi, E., Ahmad, A. & Ahmad Abulilaiwi, F. A flexible optical pH sensor based on polysulfone membranes coated with pH-responsive polyaniline nanofibers. *Sensors* **16**, 986 (2016).
43. Li, J. et al. Functional photoacoustic imaging of gastric acid secretion using pH-responsive polyaniline nanoprobe. *Small* **12**, 4690–4696 (2016).
44. Hartings, M. R., Castro, N. J., Gill, K. & Ahmed, Z. A photonic pH sensor based on photothermal spectroscopy. *Sens. Actuators B* **301**, 127076 (2019).

Acknowledgements

This work was supported by the NUS NANONASH Program (NUHSRO/2020/002/413 NanoNash/LOA; R143000B43114), National Research Foundation, Prime Minister's Office, Singapore under its Competitive Research Program (CRP Award No. NRF-NRF105-2019-0003), the Natural Science Foundation of China (92159304, 82171958, 81901812), Industrial Technology Innovation Project of Suzhou (SYG201919), Science and Technology Key Project of Shenzhen (JCYJ20190812163614809, JCYJ20200109114612308), Singapore National Medical Research Council (NMRC/OFYIRG/0081/2018) and NUS ODPRT Cross-Faculty Research Fund (CFGFY20P14). We thank Z. Liu and H. Tan for technical assistance.

Author contributions

L.Y., B.H. and X.L. conceived and designed the project. X.L., B.Z., Z.S. and R.Z. supervised the project and guided the collaboration. L.Y. characterized the materials and conducted numerical simulations. C.L. and B.X. performed electrical device fabrication. Z.S., B.H., D.H., Z.L. and D.G. performed in vivo experiments. B.H. and L.Y. performed luminescence measurements and experimental validation. J.-W.W. and C.N.L. contributed to the device design. B.H. and L.Y. wrote the manuscript. B.H., L.Y. and X.L. edited the manuscript. All authors participated in the discussion and analyses reported in the manuscript.

Competing interests

The authors declare no competing interests.

Additional information

Extended data is available for this paper at <https://doi.org/10.1038/s41551-023-01024-2>.

Supplementary information The online version contains supplementary material available at <https://doi.org/10.1038/s41551-023-01024-2>.

Correspondence and requests for materials should be addressed to Zonghai Sheng, Bin Zhou or Xiaogang Liu.

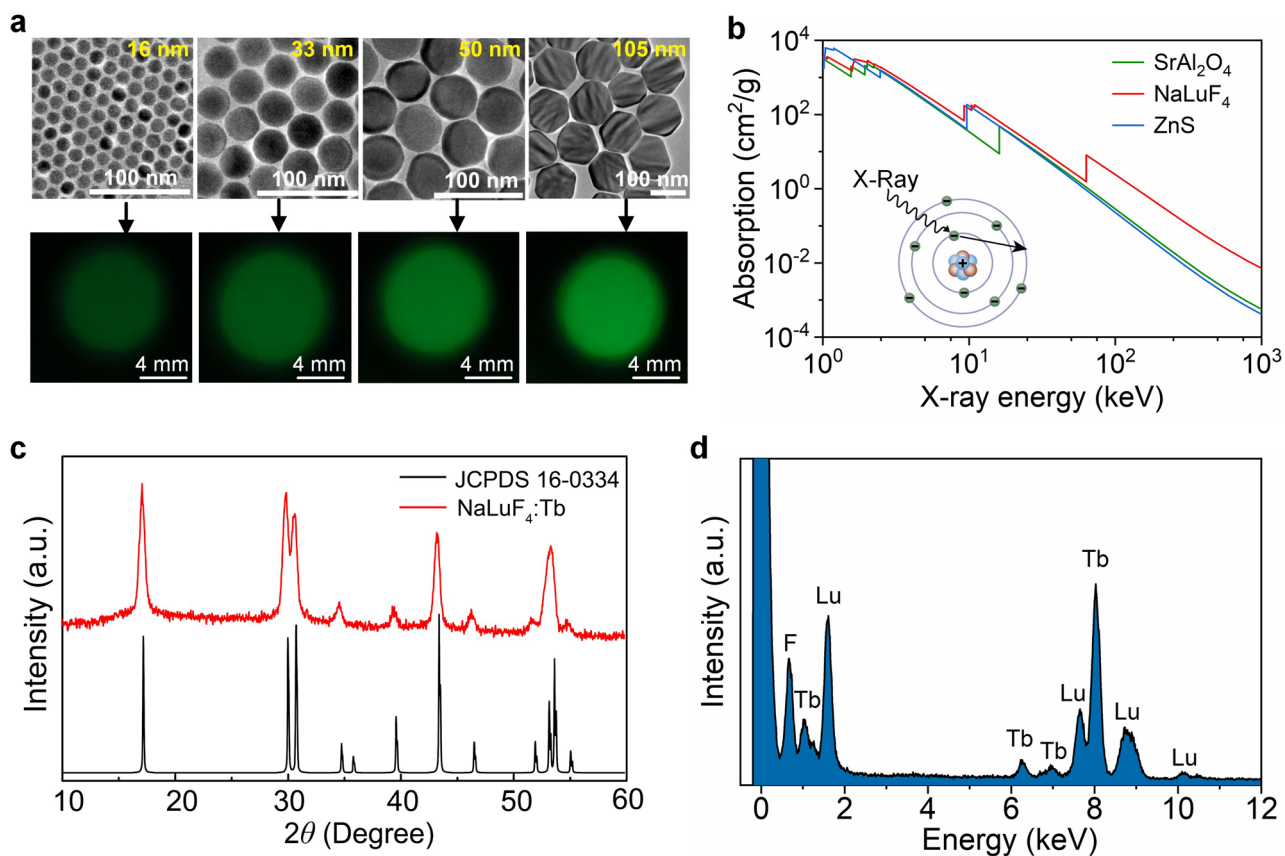
Peer review information *Nature Biomedical Engineering* thanks Louis Archambault, Christopher Bettinger, David Gladstone and Kyoungtae Lee for their contribution to the peer review of this work.

Reprints and permissions information is available at www.nature.com/reprints.

Publisher's note Springer Nature remains neutral with regard to jurisdictional claims in published maps and institutional affiliations.

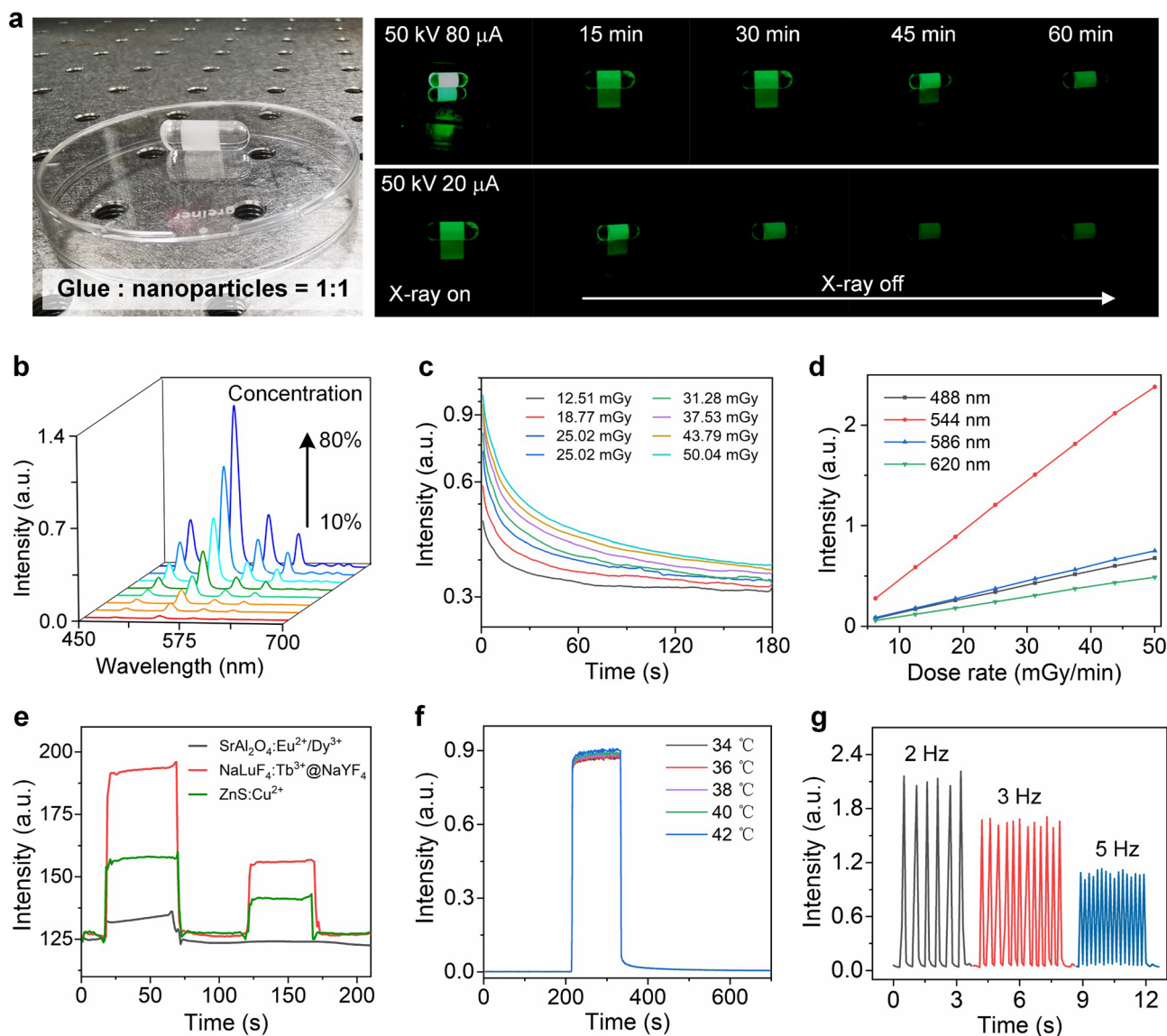
Springer Nature or its licensor (e.g. a society or other partner) holds exclusive rights to this article under a publishing agreement with the author(s) or other rightsholder(s); author self-archiving of the accepted manuscript version of this article is solely governed by the terms of such publishing agreement and applicable law.

© The Author(s), under exclusive licence to Springer Nature Limited 2023



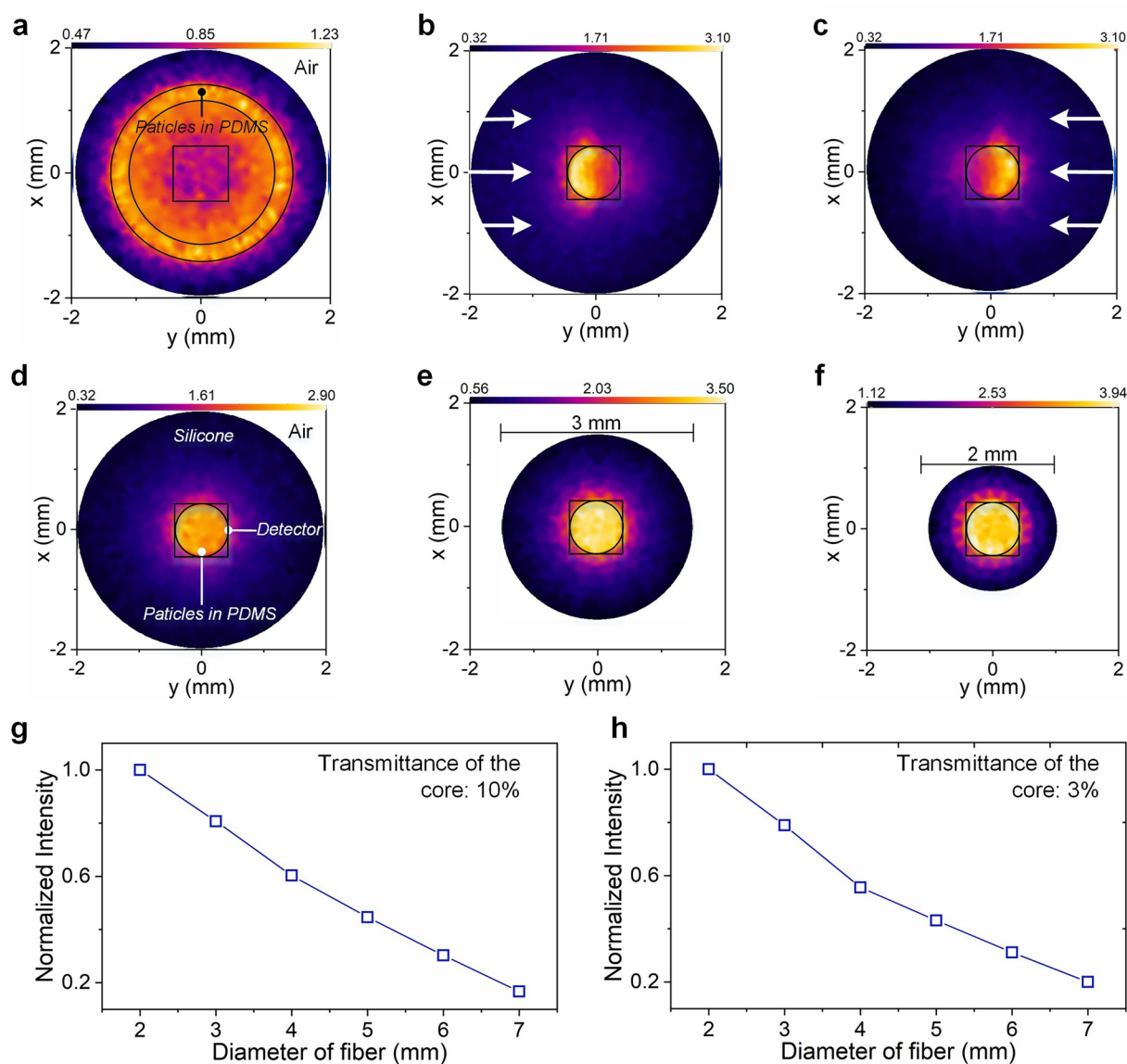
Extended Data Fig. 1 | Synthesis and characterization of Tb³⁺-doped X-ray scintillation nanocrystals. **a**, TEM images of hexagonal-phase NaLuF₄:Tb nanocrystals synthesized in various sizes (top) and corresponding radioluminescence images (bottom). **b**, X-ray energy-dependent absorption spectra of SrAl₂O₄, ZnS, and NaLuF₄. Attenuation coefficients were obtained from

ref. 39. The inset shows a schematic of X-ray-induced photoionization. **c**, Powder X-ray diffraction patterns of NaLuF₄:Tb nanocrystals. All peaks are consistent with the hexagonal-phase NaLuF₄ structure (Joint Committee on Powder Diffraction Standards (PDF) file number 27-0726, <https://github.com/yly1994/Swallowable-X-ray-Dosimeter-.git>). **d**, EDX spectra of NaLuF₄:Tb nanocrystals.



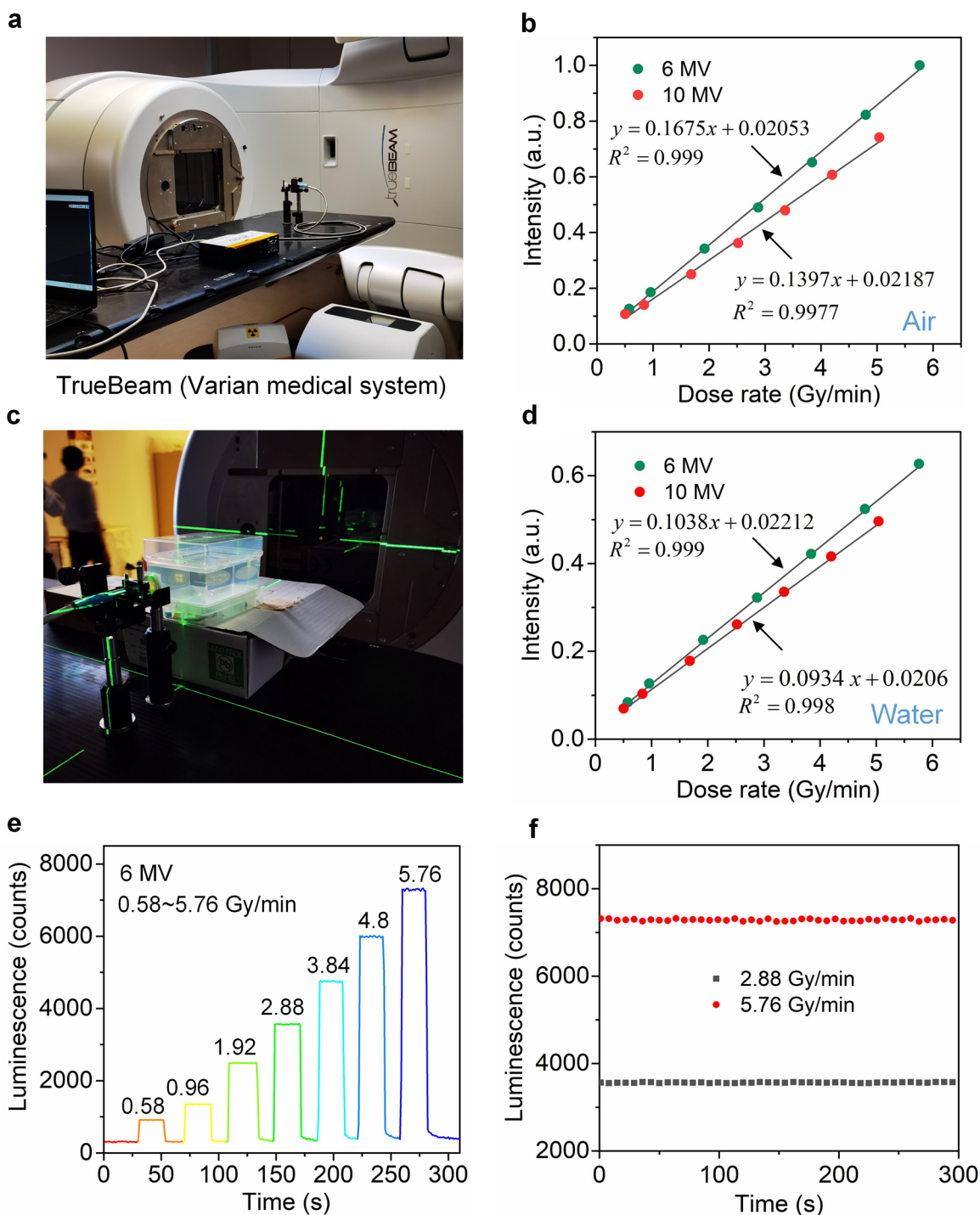
Extended Data Fig. 2 | Characterization of the NaLuF₄:Tb@NaYF₄-embedded optical fibre. **a**, Radioluminescence and afterglow photographs of NaLuF₄:Tb@NaYF₄ (15 mol%) nanocrystals embedded in an optical fibre. X-ray operation was set to 50 kV, with tube currents of 80 µA (16.68 mGy/min) and 20 µA (4.17 mGy/min). **b**, Radioluminescence spectra of the fibre embedded with NaLuF₄:Tb@NaYF₄ (15 mol%) nanocrystals of different doping concentrations. **c**, Decay curves of NaLuF₄:Tb@NaYF₄ (15 mol%) nanocrystals after exposure to various X-ray

doses at room temperature. **d**, Radioluminescence intensity versus dose rate at different wavelengths. **e**, Comparison of radioluminescence of various X-ray scintillators after termination of X-ray irradiation (50 kV and 5 kV). **f**, Time-dependent X-ray luminescence intensity at various temperatures. **g**, Radioluminescence intensity of NaLuF₄:Tb@NaYF₄ nanocrystals when irradiated with X-rays at 2, 3 and 5 Hz.



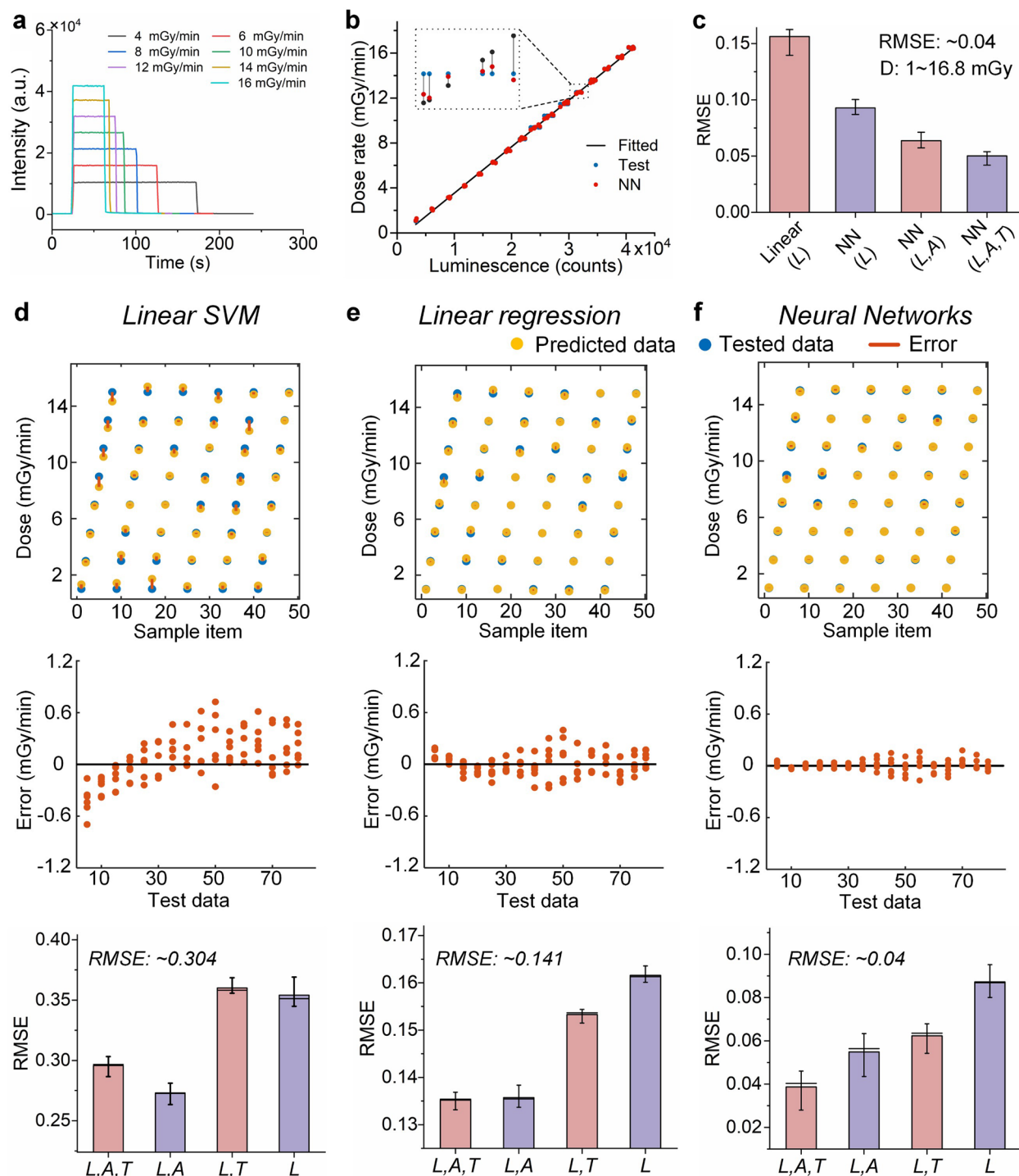
Extended Data Fig. 3 | Comparison of optical fibre designs with various geometric dimensions. **a**, Light intensity distribution of the end of an optical fibre made of thermoplastic silicone with a radius of 2 mm and a length of 8 mm, in which a cylindrical ring made of a luminescent material with a thickness of 300 μm is embedded. **b** and **c**, Simulations of an optical fibre containing a cylindrical luminescent core with a diameter of 1 mm and irradiated with X-rays from the

left (**b**) and right (**c**) sides, respectively. **d–f**, Power distribution at the fibre's end with different diameters but the same luminous core. **g** and **h**, The ratio of the intensity detected by a detector (with an area of 1 mm^2 in the centre of the fibre) and the diameter of the fibre when the luminescent core transmittance is 10% (**g**) and 3% (**h**), respectively.



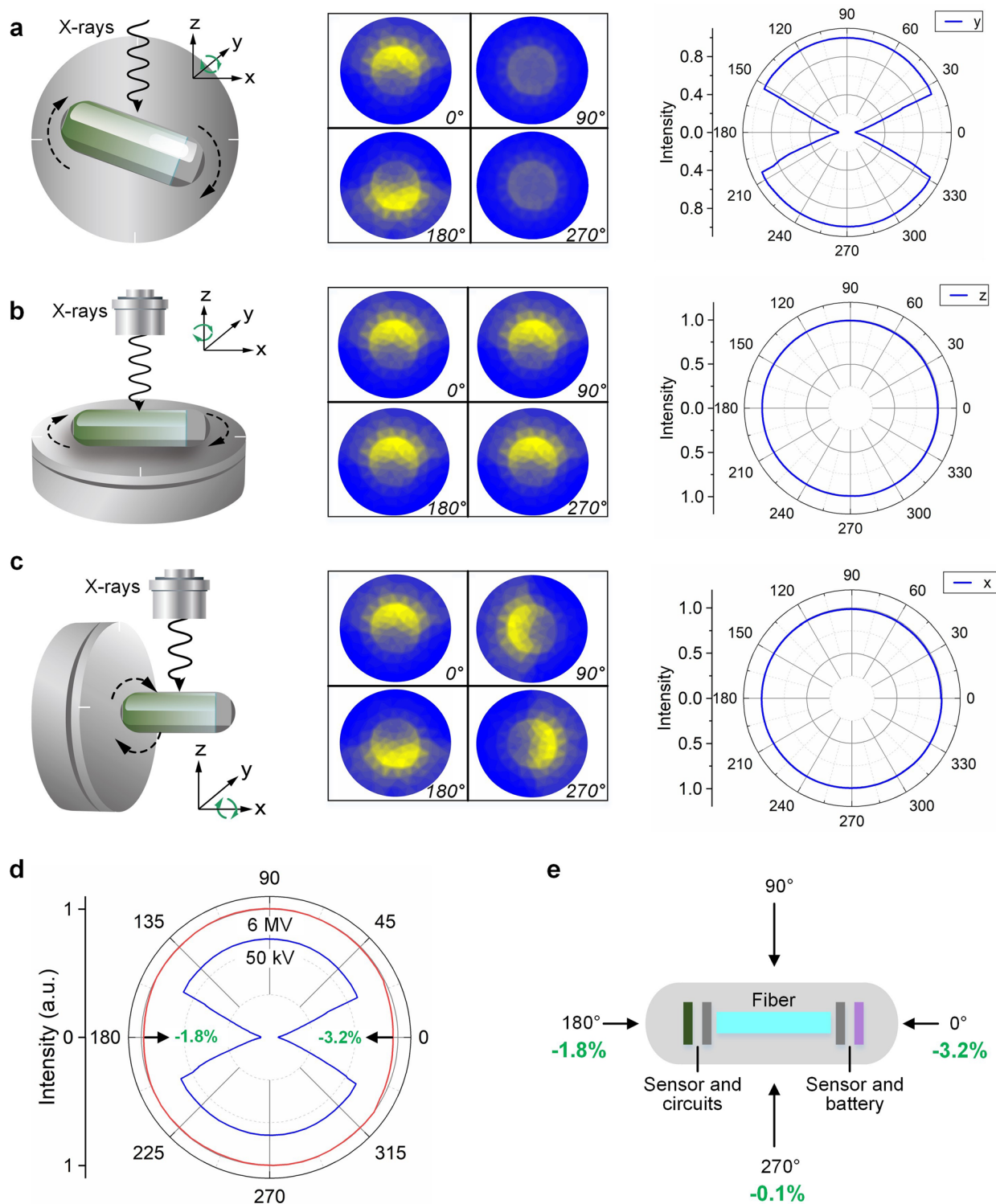
Extended Data Fig. 4 | Characterization of $\text{NaLuF}_4:\text{Tb}@\text{NaYF}_4$ nanoscrintillators exposed to megavoltage photon beams. **a**, Photograph of the experimental setup. **b**, Radioluminescence as a function of dose rate under 6 MV and 10 MV irradiation. **c**, Photograph of the experimental setup with a water tank containing water approximately 11 cm thick. **d**, Radioluminescence as a

function of dose rate under 6 MV and 10 MV irradiation with a water tank at the front. **e**, Measured radioluminescence intensity over time at dose rates from 0.58 to 5.76 Gy/min. **f**, Radioluminescence of the nanoscrintillators irradiated for 5 min at dose rates of 2.88 Gy/min and 5.76 Gy/min.



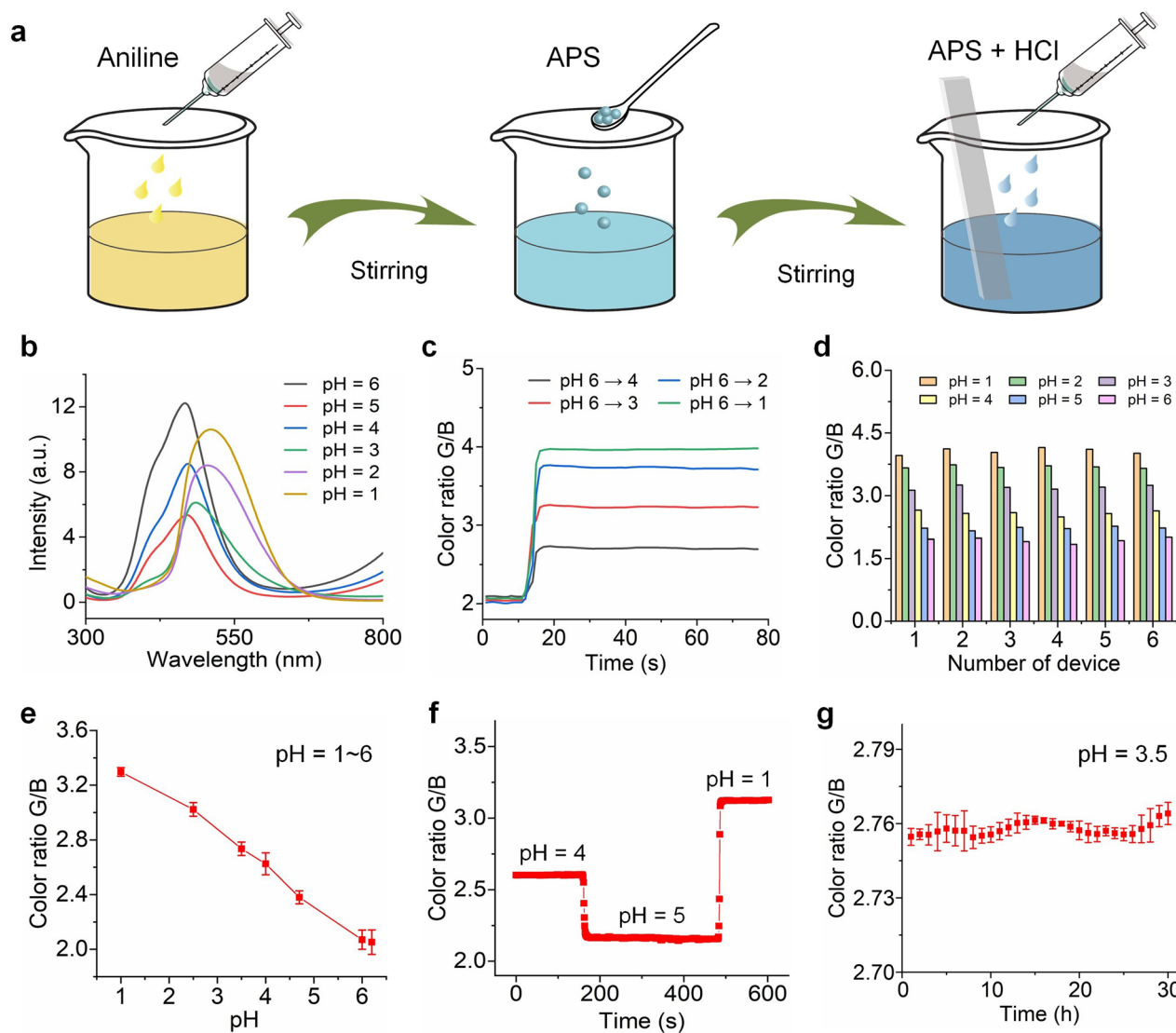
Extended Data Fig. 5 | Comparison of results from linear support vector machine (SVM), linear regression, and neural network (NN) regression. **a**, Measured radioluminescence intensity over time at a dose of 10 mGy and dose rates from 4 to 16 mGy/min. **b** and **c**, Comparison of the accuracy of dose estimation using different algorithms and feature parameter selection approaches, respectively. **d–f**, Regression results using linear SVM (**d**), linear regression (**e**), and the NN regression algorithm (**f**), with prediction-true value

scatter plots (top panels), residual plots (middle panels) and RMSE under different feature strategies (bottom panels). When radioluminescence intensity (L), afterglow intensity (A) at different times, and temperature (T) are selected as feature parameters of the regression algorithms, the RMSE of the three algorithms is 0.304, 0.141, and 0.04 mGy/min, respectively. The RMSE statistics for each algorithm are derived from 200 executions. In **c–f**, bar plots and error bars show the mean \pm s.d.



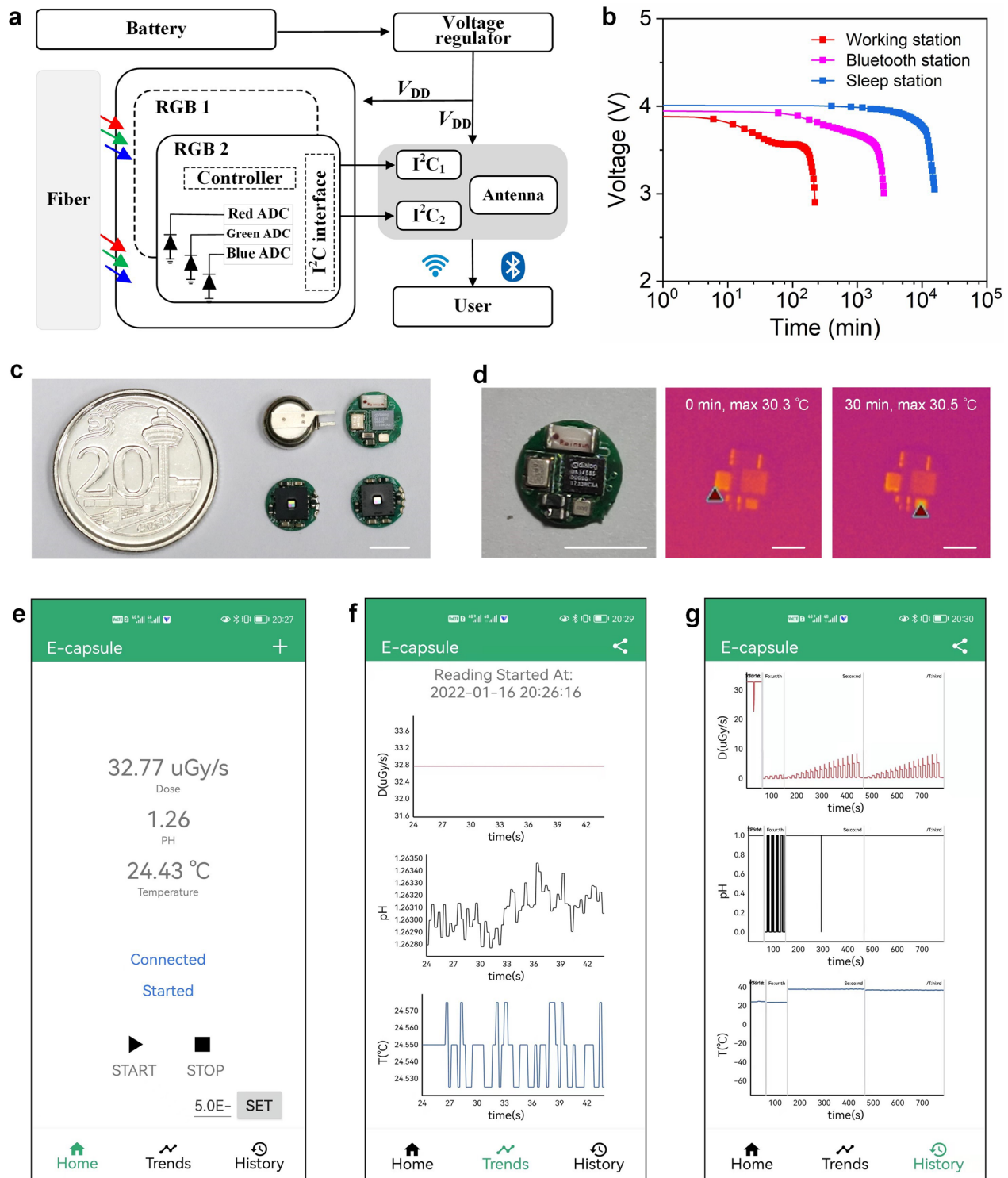
Extended Data Fig. 6 | Effect of the relative direction of the capsule and the X-rays on the radioluminescence intensity. The test schematic (left column), the simulated power distribution of the fibre end (middle column), and the power detected by the detector (right column), with X-rays incident along the z-axis

and the capsule rotating about the y-axis (a), the z-axis (b), and the x-axis (c). **d.** Power detected by the sensor versus angle of rotation of the capsule around the y-axis for a 50 kV or 6 MV beam. **e.** Average percent angular dependence of the dosimeter for different beam angles.



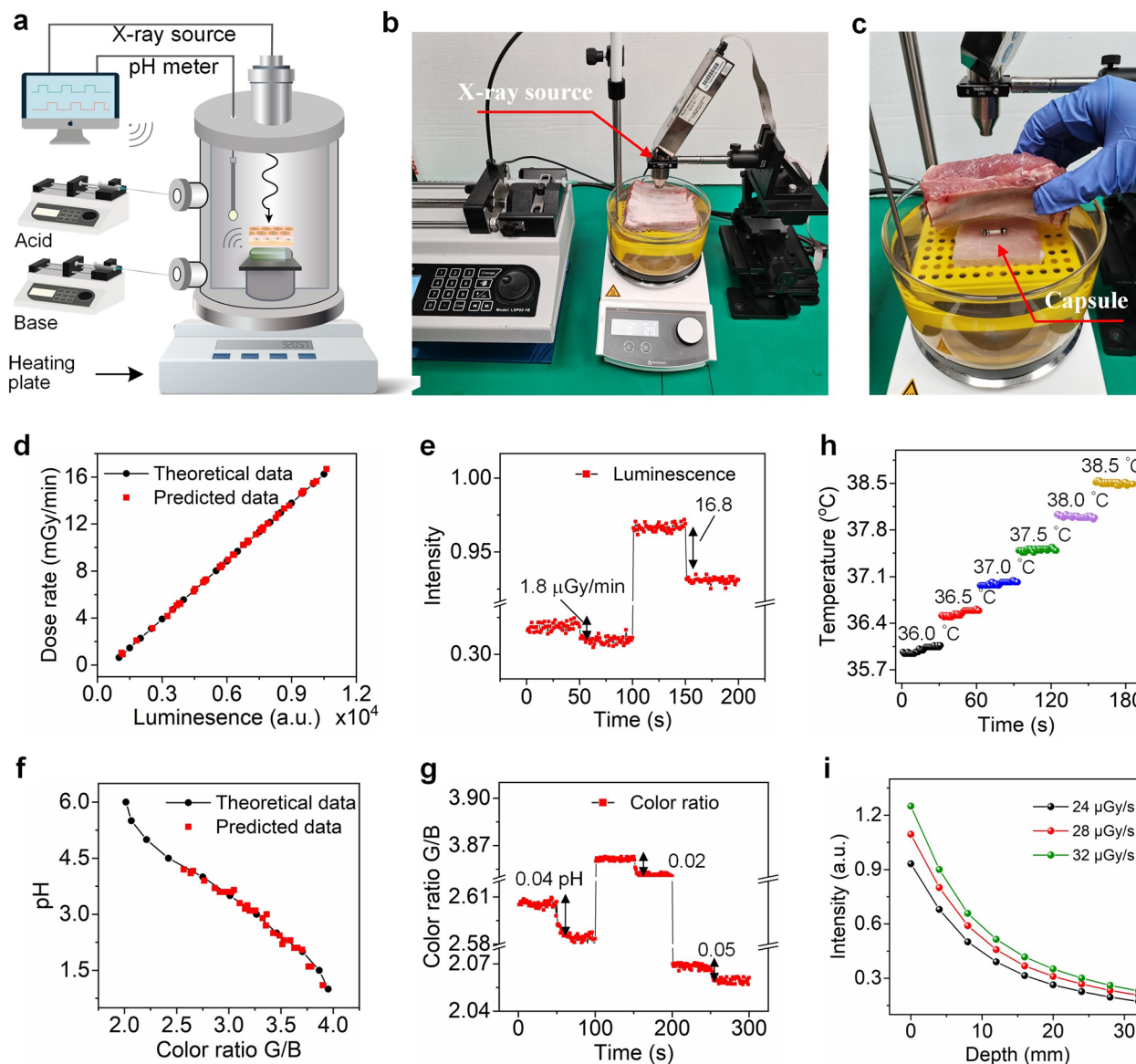
Extended Data Fig. 7 | Synthesis and characterization of the optical pH sensor. **a**, Schematic of the polyaniline synthesis. In a typical procedure, aniline liquid and ammonium persulfate (APS) were added to hydrochloric acid, followed by the addition of a PDMS substrate to the solution. **b**, Normalized transmission spectra of the pH-sensing film at various pH levels, with emission ranging from 300 nm to 800 nm. **c**, Changes in G/B colour ratio versus pH. **d**, pH

response of various devices fabricated from the same batch of polyaniline films. **e**, G/B colour ratio of the transmitted afterglow through the polyaniline film at different pH levels. **f**, Dynamic characteristics of pH sensing with afterglow. **g**, G/B colour ratio as a function of time at pH 3.5. In **e** and **g**, error bars show the s.d. of colour ratios.



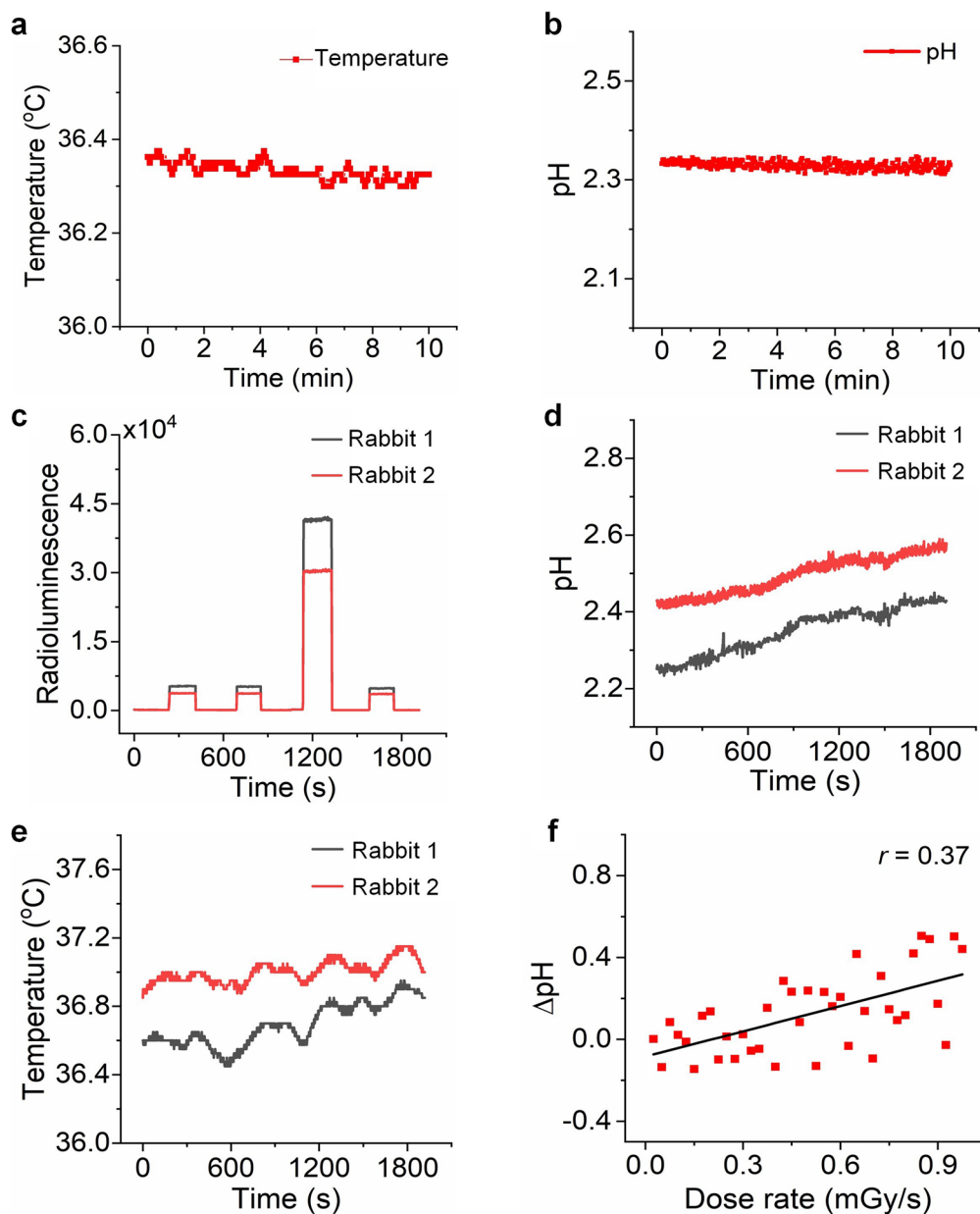
Extended Data Fig. 8 | Circuit design and characteristics, as well as the mobile application. a, System-level block diagram showing signal conversion, processing, and wireless transmission from sensors to user interface. To extend battery life, the system is designed to include a sleep state, a Bluetooth state, and a work state, with the Bluetooth chip in the sleep state the majority of the time. Power consumption in each state was $6.3 \mu\text{W}$ ($1.9 \mu\text{A}$, 3.3 V), $660 \mu\text{W}$ ($200 \mu\text{A}$, 3.3 V), and 9.57 mW (2.9 mA , 3.3 V). **b**, The battery voltage changes over time in

each of the three operating modes. **c**, Photographs of the printed circuit boards. The circuit, which has a thickness of $200 \mu\text{m}$ and a diameter of 7 mm , is easily assembled and fits well into a standard size 2 capsule. **d**, Thermal images of the circuit board after various times of operation. Circuit heating was less than $0.2 \text{ }^\circ\text{C}$ after 30 min of operation. The scale bar is 5 mm . **e**, The application's homepage prior to Bluetooth pairing. **f**, Real-time display of representative data from the capsule. **g**, Historical data analysis and display.



Extended Data Fig. 9 | In vitro experimental setup, as well as dose and pH calibration and resolution testing. **a**, Capsule operation in distilled water. The water tank was placed on a stirring hot plate to keep the solution temperature between 32 °C and 46 °C. The pH was measured with a commercial pH meter and varied by controlling the ratio of HCl and NaOH supplied to the tank via a microsyringe pump. **b**, Photograph of the experimental setup used for *in vitro* demonstration of the capsule. **c**, Photograph of the capsule operating wirelessly under a fresh *ex vivo* porcine bone sample. **d**, Calibration of the relationship between the dose delivered to the capsule and radioluminescence. The data show excellent linearity, with an average accuracy error of less than 0.5%.

e, Radioluminescence intensity at different dose rates. The minimum detectable dose rate difference was 1.8 $\mu\text{Gy}/\text{min}$. **f**, Calibration of the relationship between pH and the G/B colour ratio. The average accuracy error is approximately 0.13. **g**, G/B colour ratio at different pH values. The minimum detectable pH difference was 0.02, corresponding to a difference of 0.009 in sensor output colour ratio. **h**, Temperature change measured by the capsule from 36 °C to 38.5 °C in 0.5 °C intervals. It should be noted that the sensor needs to be calibrated before it can be used to measure absolute temperature. **i**, Response measurements of the capsule under different thicknesses of fresh *ex vivo* porcine samples at different dose rates.

**Extended Data Fig. 10 | Irradiation administration via the capsule.**

a, Temperature change recorded by the capsule over time in a stable experimental environment. **b**, Change in capsule pH over time, as measured by the persistent luminescence of NaLuF₄:Tb@NaYF₄ nanoscintillators. **c–e**, Time-

course results of the absorbed dose, pH, and temperature of different capsules in two rabbits. **f**, Correlation between dose rate and pH changes. The correlation coefficient was obtained by linear fitting.

Reporting Summary

Nature Portfolio wishes to improve the reproducibility of the work that we publish. This form provides structure for consistency and transparency in reporting. For further information on Nature Portfolio policies, see our [Editorial Policies](#) and the [Editorial Policy Checklist](#).

Statistics

For all statistical analyses, confirm that the following items are present in the figure legend, table legend, main text, or Methods section.

n/a Confirmed

- The exact sample size (n) for each experimental group/condition, given as a discrete number and unit of measurement
- A statement on whether measurements were taken from distinct samples or whether the same sample was measured repeatedly
- The statistical test(s) used AND whether they are one- or two-sided
Only common tests should be described solely by name; describe more complex techniques in the Methods section.
- A description of all covariates tested
- A description of any assumptions or corrections, such as tests of normality and adjustment for multiple comparisons
- A full description of the statistical parameters including central tendency (e.g. means) or other basic estimates (e.g. regression coefficient) AND variation (e.g. standard deviation) or associated estimates of uncertainty (e.g. confidence intervals)
- For null hypothesis testing, the test statistic (e.g. F , t , r) with confidence intervals, effect sizes, degrees of freedom and P value noted
Give P values as exact values whenever suitable.
- For Bayesian analysis, information on the choice of priors and Markov chain Monte Carlo settings
- For hierarchical and complex designs, identification of the appropriate level for tests and full reporting of outcomes
- Estimates of effect sizes (e.g. Cohen's d , Pearson's r), indicating how they were calculated

Our web collection on [statistics for biologists](#) contains articles on many of the points above.

Software and code

Policy information about [availability of computer code](#)

- | | |
|-----------------|---|
| Data collection | The material luminescence response was recorded using a fiber optic spectrometer (Ocean Optics QE Pro) and Edinburgh FS5 fluorescence spectrophotometer (Edinburgh Instruments Ltd, U.K.). Transmission spectra of the pH sensor film in solutions with different pH values were measured using a spectrophotometer (Cary Series UV-Vis-NIR, Agilent). Data were collected using a Dialog Semiconductor microcontroller DA14585 and visual studio 2015. Custom application codes used for data analysis and display in this paper can be found at https://github.com/yly1994/Swallowable-X-ray-Dosimeter-git |
| Data analysis | MATLAB 2020 (Regression Learner and Neural Network Fitting application toolboxes) for data analysis, COMSOL Multiphysics 5.6 for simulation. |

For manuscripts utilizing custom algorithms or software that are central to the research but not yet described in published literature, software must be made available to editors and reviewers. We strongly encourage code deposition in a community repository (e.g. GitHub). See the Nature Portfolio [guidelines for submitting code & software](#) for further information.

Data

Policy information about [availability of data](#)

All manuscripts must include a [data availability statement](#). This statement should provide the following information, where applicable:

- Accession codes, unique identifiers, or web links for publicly available datasets
- A description of any restrictions on data availability
- For clinical datasets or third party data, please ensure that the statement adheres to our [policy](#)

The main data supporting the results in this study are available within the paper and its Supplementary Information. All data generated in this study, including source data and the data used to make the figures, are available for research purposes from the corresponding author on reasonable request.

Field-specific reporting

Please select the one below that is the best fit for your research. If you are not sure, read the appropriate sections before making your selection.

- Life sciences Behavioural & social sciences Ecological, evolutionary & environmental sciences

For a reference copy of the document with all sections, see [nature.com/documents/nr-reporting-summary-flat.pdf](https://www.nature.com/documents/nr-reporting-summary-flat.pdf)

Life sciences study design

All studies must disclose on these points even when the disclosure is negative.

Sample size	We first performed in vitro validation experiments for the accuracy and sensitivity of dose, pH and temperature (Extended Data Fig. 9). The animal experiments were performed to demonstrate the capabilities of the capsule. We determined sample sizes and the number of animals for these in vitro and in vivo experiments on the basis of similar prior studies (refs. 9, 32). We used a total of twelve male rabbits during the testing of the system. Three were used for the stability test of the device, three were used for the angle-dependence test, and 12 were used for the routine blood test. Some rabbits were used in multiple tests on the basis of the reasonable principle of controlled experiments.
Data exclusions	No data were excluded.
Replication	All attempts at replication were successful. In the in vitro testing of the devices (Fig. 4e), the pH, temperature and dose rate tests were repeated 3 times every 16 hours. During in vivo testing of the device, the dose rate test was repeated hourly for a total of 10 repetitions (Fig. 5c), and the pH test was repeated 15 times per minute (Fig. 4d). The angle dependence was replicated using three rabbits (Fig. 4c).
Randomization	Randomization was not relevant for the study, because comparisons of effects between rabbits were not part of it. All rabbits used for the control experiments were of the same type and handled in the same way.
Blinding	Data collection and analysis for each rabbit were performed by different researchers. The personnel completing the data analyses were blinded to the experimental groups.

Reporting for specific materials, systems and methods

We require information from authors about some types of materials, experimental systems and methods used in many studies. Here, indicate whether each material, system or method listed is relevant to your study. If you are not sure if a list item applies to your research, read the appropriate section before selecting a response.

Materials & experimental systems

n/a	Included in the study
<input checked="" type="checkbox"/>	<input type="checkbox"/> Antibodies
<input checked="" type="checkbox"/>	<input type="checkbox"/> Eukaryotic cell lines
<input checked="" type="checkbox"/>	<input type="checkbox"/> Palaeontology and archaeology
<input type="checkbox"/>	<input checked="" type="checkbox"/> Animals and other organisms
<input checked="" type="checkbox"/>	<input type="checkbox"/> Human research participants
<input checked="" type="checkbox"/>	<input type="checkbox"/> Clinical data
<input checked="" type="checkbox"/>	<input type="checkbox"/> Dual use research of concern

Methods

n/a	Included in the study
<input checked="" type="checkbox"/>	<input type="checkbox"/> ChIP-seq
<input checked="" type="checkbox"/>	<input type="checkbox"/> Flow cytometry
<input checked="" type="checkbox"/>	<input type="checkbox"/> MRI-based neuroimaging

Animals and other organisms

Policy information about [studies involving animals](#); [ARRIVE guidelines](#) recommended for reporting animal research

Laboratory animals	Adult male New Zealand white rabbits (90 days old, 1.8~2.2 kg).
Wild animals	The study did not involve wild animals.
Field-collected samples	The study did not involve samples collected from field.
Ethics oversight	All animal experiments were conducted according to the protocol approved by Shenzhen Institute of Advanced Technology, Chinese Academy of Sciences Animal Care and Use Committee.

Note that full information on the approval of the study protocol must also be provided in the manuscript.